UC San Diego
UC San Diego Previously Published Works

Title

Functional organization of posterior parietal cortex circuitry based on inferred information flow.

Permalink

Journal

Authors

Kang, Jung
Mooshagian, Eric
Snyder, Lawrence

Publication Date

DOI

Peer reviewed

Functional organization of posterior parietal cortex circuitry based on inferred information flow

Jung Uk Kang[1,2,5,*], **Eric Mooshagian**[1,3,4,5], **Lawrence H. Snyder**[1,6]

[1]Department of Neuroscience, Washington University School of Medicine, St. Louis, MO 63110, USA

[2]Present address: Department of Neurosurgery, Baylor College of Medicine, Houston, TX 77030, USA

[3]Present address: Department of Cognitive Science, University of California, San Diego, La Jolla, CA 92093, USA

[4]Present address: Systems Neurobiology Laboratories, The Salk Institute for Biological Studies, La Jolla, CA 92037, USA

[5]These authors contributed equally

[6]Lead contact

SUMMARY

Many studies infer the role of neurons by asking what information can be decoded from their activity or by observing the consequences of perturbing their activity. An alternative approach is to consider information flow between neurons. We applied this approach to the parietal reach region (PRR) and the lateral intraparietal area (LIP) in posterior parietal cortex. Two complementary methods imply that across a range of reaching tasks, information flows primarily from PRR to LIP. This indicates that during a coordinated reach task, LIP has minimal influence on PRR and rules out the idea that LIP forms a general purpose spatial processing hub for action and cognition. Instead, we conclude that PRR and LIP operate in parallel to plan arm and eye movements, respectively, with asymmetric interactions that likely support eye-hand coordination. Similar methods can be applied to other areas to infer their functional relationships based on inferred information flow.

Graphical Abstract
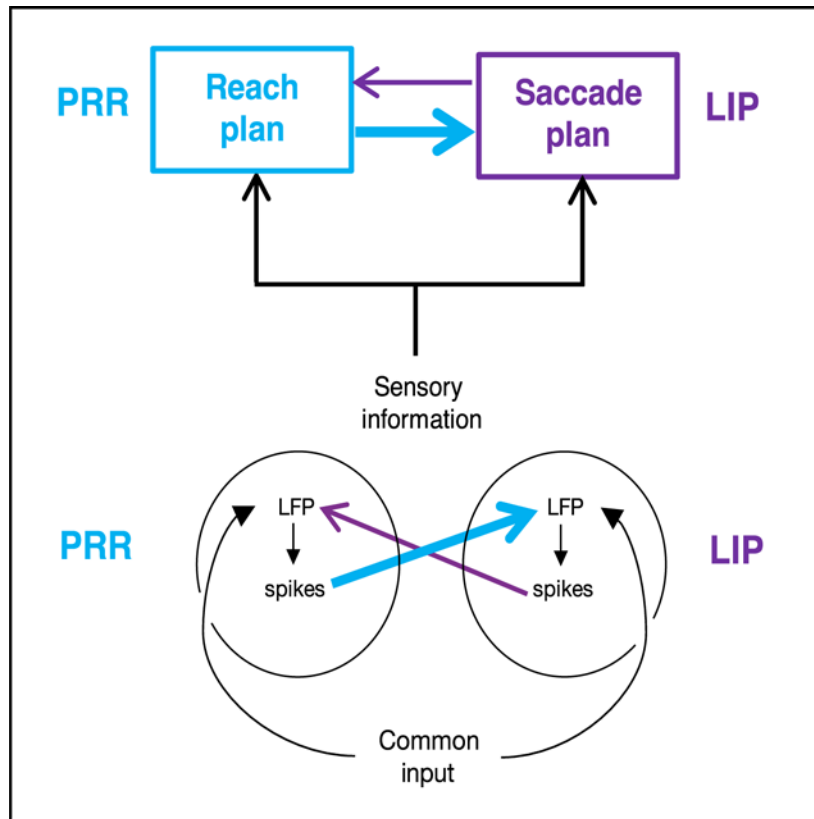
In brief

Kang et al. demonstrate that during eye-hand coordination tasks, the parietal reach region (PRR) and the lateral intraparietal area (LIP) operate in parallel to plan arm and eye movements, respectively. They show asymmetric interactions between the PRR and LIP, with information flowing primarily from the PRR to LIP.

INTRODUCTION

There is a rich history of identifying modules within the brain and assigning roles to them based either on what function(s) are perturbed following an intervention or by what information their neurons encode.[1–5] An alternative approach is to consider information flow, which can be assayed based on anatomical or functional measures.[6–11] Knowing whether functional connectivity is causal or merely correlative, and whether the connectivity depends on the task at hand, is critical to inferring functional relationships.[12–17]

Individual parietal areas have been associated with particular effectors and types of movement. The anterior intraparietal area is associated with grasping movements,[18–20] the medial superior temporal area with pursuit eye movements,[21,22] and the parietal reach region (PRR) with reaching movements.[23,24] The lateral intraparietal area (LIP) has been proposed to be an exception to this general rule. Although it is clearly associated with saccadic eye movements,[25–28] it has been argued that LIP serves high-level roles in multiple spatial cognition tasks.[29–39] To account for these high-level roles, it has been proposed that LIP

forms a "priority map" of space, identifying important spatial locations and then propagating that information to other areas, including PRR, to further cognitive or motor goals (Figure 1A, spatial hub or priority map model).[29,31,40] With this model, eye-hand coordination is accomplished by virtue of one area, LIP, specifying targets for both eye and arm movements.

An alternative model is based on evidence of effector specificity in LIP and PRR,[24,27,43–50] plus the fact that in normal behavior, saccades and reaches are often decoupled.[51] Although attention is tightly linked to gaze in simple saccade tasks and reach tasks,[52–54] decoupling the eye and arm unmasks distinct spatial processing, including independent attention-like phenomenon, in the saccade and reach systems.[55–58] This suggests a decentralized or parallel model of eye and arm movements (Figure 1B, parallel model), with LIP handling saccadic eye movements and PRR independently handling reaches. In this model, eye-hand coordination occurs when PRR and LIP independently settle on the same target of interest. When this does not occur, movements are decoupled, unless downstream pathways explicitly modify eye-hand coordination.[44] A third model adds direct interactions between PRR and LIP (Figure 1C, parallel with interactions), providing a means for coordination at the level of these areas.[43,44,47,49,59–62] Although it is often helpful to look where we reach, the reverse—reaching to where we look—can be wasteful, offensive, and even dangerous, depending on the situation. When we look someone in the eye, we do not want to also poke them in the eye. Therefore, connections between the two pathways would likely be asymmetric, with more influence of reaching on saccades than vice versa.

The three models, spatial hub, parallel, or parallel with asymmetric interactions, are distinguished by the direction of information flow between PRR and LIP during coordinated eye and arm movement tasks. In this study, we considered the temporal relationships between action potentials (spikes) and local field potentials (LFP) as well as LFP-LFP relationships.[17,63] We find that in the delay period before a coordinated eye and arm movement, information flows mostly from PRR to LIP, with at best only a small amount of flow from LIP to PRR. This is not consistent with a spatial hub model and points instead to a parallel processing model with asymmetric connections that serve eye-hand coordination.

RESULTS

We recorded single units and LFP from PRR and LIP in both hemispheres of two monkeys to quantify functional connectivity related to the planning of eye and arm movements. Single-unit activity and LFP power from PRR and LIP are shown in Figure S1. Details of the electrophysiological data are provided in previously published studies.[45,46,62] Animals reached with the left hand (unimanual), right hand (unimanual), or both hands together (bimanual-together) to a single target or moved each hand to a different target (bimanual-apart) (Figure 2A). Animals made saccades to the reach targets on most trials. For single-target trials, a saccade to the target was required, whereas for bimanual-apart trials, animals were free to move their eyes as they chose. In a fifth trial type, animals made a saccade without a reach (saccade-only). All trial types were interleaved. On each trial, animals were instructed to prepare the appropriate movement based on the color of the peripheral target(s) and then cued to initiate that movement after a variable delay period of 1,250–1,750 ms. Overall performance following training was good—86% of initiated trials (two home

buttons touched and initial fixation target acquired) were successfully completed. Saccades slightly preceded unimanual reaches, with median reaction times (RTs) of 217 and 328 ms, respectively. Bimanual reaches were initiated roughly synchronously, with a median absolute difference in the two arms' RTs of 31 and 30 ms, for bimanual-together and bimanual-apart trials, respectively.

Inferred information flows primarily from PRR to LIP during the movement planning period

We assayed directional information flow between PRR and LIP using two largely independent methods: time-lagged spike-LFP coherence and LFP-LFP spectral Granger causality.[17,64,65] We first focus on spike-LFP coherence in the movement planning period, the 800-ms interval before the go cue. This interval contains no changes in task-related stimuli that would produce visual responses and no task-related responses that would produce proprioceptive feedback, either of which could drive confounding common input to both PRR and LIP. We are particularly interested in information flow in the beta band (15–40 Hz) because it has been implicated in motor planning.[46,66] We use "coherence from A to B" as shorthand for the coherence between spikes in location A with LFP in location B because we expect that spikes in one area more directly drive LFP in another area than vice versa (see Discussion). Within a single hemisphere, coherence from PRR to LIP (Figure 2B; blue trace) is significantly elevated above chance levels at 10–64 Hz. At 25–45 Hz, coherence from PRR to LIP is more than twice as large as coherence from LIP to PRR (purple trace) relative to chance levels (pooled t test, $p < 0.001$ at each frequency). Information flow may differ for across-hemisphere compared to within-hemisphere, so we tested both conditions. We find similar asymmetries in both cases, although coherence magnitudes for across-hemisphere are reduced compared to within-hemisphere recording sites (Figure 2C). The larger distance between across-hemisphere compared to within-hemisphere recording sites may reduce artifactual common input due to direct effects of LFP across sites, but should not affect the magnitude of the asymmetry. The results therefore confirm that coherence from PRR to LIP is greater than from LIP to PRR and indicate that within-hemisphere flow is greater than across-hemisphere flow. The same asymmetry can also be found with alternatives to coherence (e.g., pairwise phase consistency, an unbiased measure of spike-field synchronization that is robust to differences in spike counts) (Figure S2A).[67]

Next, we computed spectral Granger causality between LFPs. Measures of functional connectivity based on LFP-LFP interactions will not necessarily be the same as those based on spike-LFP interactions. However, finding similar directional asymmetries across two independent measures would increase confidence in the results.[68] We use "Granger causality from A to B" as a shorthand for how well LFP from location B can be predicted using LFP from location A. Like spike-LFP coherence, spectral Granger causality is greater from PRR to LIP than from LIP to PRR (within hemisphere, Figure 2D; across hemisphere, Figure 2E). The directional asymmetry is highly significant at 19–27 Hz (Wilcoxon signed rank test, $p < 0.001$ at each frequency). Importantly, this directional asymmetry is not an artifact of greater power in one region than the other (Figure S3).[69–71] Similar results for both spike-LFP and Granger causality analyses were found when data from each animal were analyzed separately (Figure S4).

Inferred information flow from PRR to LIP is task specific

The data in Figure 2 were computed after combining responses to all four interleaved reach trial types. Finding differences in measures of information transfer such as magnitude and peak frequencies across tasks would be consistent with the transmission of task-relevant information. Indeed, unimanual and bimanual reaches were each associated with unique spike-LFP coherence spectra (Figure 3A). Within a single hemisphere, the two bimanual tasks were associated with the strongest coherence (0.091) and peaked at 35 Hz. The two unimanual tasks were associated with an intermediate level of coherence and a lower peak (0.087) at 30 Hz. There was significant task specificity at 27–40 Hz (repeated-measures ANOVA, $p < 0.001$ at each frequency). We observed similar, although not identical, task specificity using different time-frequency bandwidths (data not shown) and with pairwise phase consistency (Figure S2B). Cross-hemispheric coherence from PRR to LIP also showed a similar pattern of task specificity (Figure S5). In contrast, coherence from LIP to PRR was not significantly affected by the type of reach (Figure 3B). In fact, the coherence from LIP to PRR during reach preparation was barely above the shuffle confidence limits. A similar result is obtained through spectral Granger causality analysis of LFP signals; there is significant task-specific modulation from PRR to LIP at 19–27 Hz but not from LIP to PRR at any frequency (Figures 3C and 3D, permutation test, $p < 0.01$).

We next considered information flow when animals were planning a saccade-only movement compared to a reach plus a saccade (Figure 4). Shared information is greater from PRR to LIP for reaches plus saccades compared to saccade-only movements, although the effect was significant only for Granger causality (Figure 4C). Spike-LFP coherence is higher for saccades than reaches at low frequencies, but the effect is not significant and is not replicated in the Granger causality analysis. Our statistical power is limited in these analyses, however, by the small number of saccade-only trials (25% as many as reach trials) and, given the lower activity for saccade compared to reach trials in PRR (Figure S1E), by the limited number of spike-LFP pairs that meet our minimum spike count criterion (see STAR Methods).

Coherence from PRR to LIP reflects a causal effect

An analysis of the temporal lag that maximizes interareal spike-LFP coherence can provide information about causal effects. Spikes from one area may drive synaptic and dendritic currents in a second area, thereby contributing to LFP in the second area.[73,74] Because spike propagation, synaptic transmission, and dendritic conduction are not instantaneous, we expect a lag between when a spike occurs in one area and when that spike exerts its peak influence on LFP in another area (Figures 5A and 5D, blue).[75] Consider an experiment in which spikes are recorded from area X, LFP is recorded from area Y, and spike-LFP coherence is computed between these two signals. If information flows from X to Y, then we expect that spike-LFP coherence would be elevated and would be greatest when the spike signal is lagged (shifted later in time) relative to the LFP signal. If information flows in the opposite direction, from Y to X, then we again expect elevated coherence. However, the path for information transfer requires more steps in the case of flow from Y to X compared to X to Y (compare Figures 5B and 5A, respectively) and so the coherence would be lower for Y to X than X to Y. Furthermore, coherence for the Y to X case should be greatest when

the spike signal is moved earlier in time (a negative lag) relative to the LFP signal (Figure 5D, orange). Finally, elevated coherence could arise from common input to both areas rather than from communication between the areas (Figure 5C). In this case, the common input will first drive LFP in both areas and then, a short time later, influence spikes in both areas. Thus, coherence will be maximized when a small lead is imposed on the spikes (Figure 5D, magenta).

We determined the temporal lag or lead that maximizes cross-areal spike-LFP coherence in each direction. From PRR to LIP, there was a clear peak in coherence at 25 Hz when a lag of 12 ms was imposed on spikes relative to LFPs (Figure 5E, cyan). We repeated this analysis across a broad range of frequencies and found that the spike lag that maximizes spike-LFP coherence ("peak lag") is significantly different from zero only at 21–36 Hz, with mean values of ~10 ms across the 5 tasks (Figure 6A). This timing is consistent with the time required for information to travel from one cortical area to another, and is also consistent with the lag previously reported for high-frequency spike-LFP coherence.[76–78] Outside of 21–36 Hz, the peak lag was inconsistent across tasks and not significantly different from zero, consistent with no transfer of information. Similar effects were seen for across-hemisphere interactions (Figure 6C). The exact value for peak lag depended on the task being planned, with lags of ~12 ms when the task included a contralateral reach and smaller values for saccades and ipsilateral reaches (Figure S6A). In the reverse direction, from LIP to PRR, peak coherence occurred with no lag or even a slight lead of ~4 ms (Figures 5E, purple, 6B, and S6B). The overall pattern is consistent with information flowing from PRR to LIP plus common input into both areas and perhaps some weak flow from LIP to PRR. This, in turn, suggests that PRR, having obtained visual information from earlier visual areas,[11] determines where a reach will be directed and then communicates that information to LIP.

Our results support the idea that information flows primarily from PRR to LIP during the movement planning period before a reach. It is possible, however, that LIP sends information about where to make arm movements to PRR shortly after the target appears, and that the subsequent flow from PRR to LIP reflects feedback to LIP. To test this possibility, we next consider information flow immediately following target presentation.

Information flow is primarily from PRR to LIP immediately after target appearance

An alternative interpretation of our data is that LIP sends information to PRR about where to make arm movements after the target appears, and that subsequent information flow, from PRR to LIP, reflects feedback to LIP. A dominant role for LIP in reaching is suggested by the fact that saccades often precede reaches, for example, by 111 ms in the present study.[79] Relative movement onset does not, however, predict the order of neuronal activation. In fact, in our task, PRR activity reflects reach direction earlier than LIP (Figure 7A). This is not wholly unexpected: eye tracking methods (e.g., eye coils or video recording) are generally more sensitive to movement onset than arm-tracking methods (e.g., capacitive switches or touch screens), arm electromyography is synchronous with the start of the saccade,[79] reach-associated spikes in M1 precede saccade-associated spikes in the oculomotor nuclei by 130 ms,[80,81] and PRR latencies are known to depend on the task being performed.[82]

In the interval from 50 to 550 ms after target onset, coherence from PRR to LIP was well above chance, but coherence from LIP to PRR was substantially smaller and only barely significant (Figure 7B). The coherence was shifted to slightly higher frequencies compared to later in the trial, with peaks at 43 Hz (PRR to LIP) and 41 Hz (LIP to PRR), but the pattern otherwise resembled the effects during the delay period. There was significant task-specific modulation from PRR to LIP (Figures S7A and S7B). Looking only at spikes associated with the preferred direction does not change this pattern (Figure S8), and looking at shorter periods starting at target onset (e.g., 50–450 ms) yields noisier but broadly similar results (Figure S9). Unlike the spike-LFP coherence result, Granger causality shows similar effects for the two directions in this early period (Figure 7B). Note, however, the 10-fold increase in permutation results compared to the permutation results from the later interval (Figure 2D) and also the fact that the elevation in Granger causality occurs at all frequencies, not just at the beta frequencies as seen in most other analyses. This is consistent with a large LFP signal in both areas, driven by target appearance and potentially masking smaller effects due to communication. It is also the case that there are early task-specific modulations for PRR to LIP but not for LIP to PRR, in both spike-LFP coherence and Granger causality LFP-LFP analyses (Figure S7). This is like the pattern seen in the late delay period, and consistent with task-specific information flowing from PRR to LIP but not from LIP to PRR.

DISCUSSION

We asked whether the relative functional organization of PRR and LIP is best described as hierarchical, with LIP providing high-order spatial information to a subordinate PRR, or parallel, with each area operating on its own and sharing information on a task-specific basis. To distinguish between these two architectures, we inferred interareal information flow across different tasks using time-lagged spike-LFP coherence and spectral Granger causality. In most analyses, inferred information flow from PRR to LIP was at least twice as large as the flow from LIP to PRR (Figures 2, 3, and 7). The time-lagged analysis strongly supports the idea that flow is primarily from PRR to LIP (Figures 5E and 6; compare with simulation results in Figures 5D and S10). Reach direction is coded in single-unit activity in PRR earlier than in LIP (Figure 7A). Inferred information flow from PRR to LIP depended on the particular type of reach being performed, but this was not the case for flow from LIP to PRR (Figures 3 and S5). This is consistent with information from PRR to LIP being used to guide accompanying eye movements whose specifics depend on the particulars of each reach. The much smaller inferred information flow from LIP to PRR could be an artifact of common input (Figure S10C) or it could help coordinate the timing of the two movements. Taken together, these results imply a parallel architecture for the planning of reaches and saccades, with asymmetric interactions that may help support eye-hand coordination.

Previous work has shown that PRR represents targets for planned arm movements, whereas LIP represents targets for planned eye movements.[23–27] Eye movements are tightly and reciprocally coupled to attention—we look at what we attend to, and our attention automatically shifts to the goal of an upcoming saccade.[83] This reciprocal relationship is evident during the planning period before an eye movement, even in peripheral attention tasks in which an eye movement is disallowed.[84] Thus, it is not surprising that LIP is active not just with saccades but also in nonsaccadic tasks involving spatial attention. Based on

such activations, it has been proposed that LIP forms a "priority map" of space,[29,31] which could then propagate behaviorally relevant spatial information to other areas to guide not just saccades but other movements as well.[35,38–40] Arm movements provide an excellent test of this proposal. Primates, including humans, often look where they will reach, and saccade and reach RTs are correlated.[79,85–88] It is known that LIP also contains information about planned arm movements.[38,89,90] It is not clear, however, whether LIP specifies the reach target or whether the decision about where to reach is made elsewhere, for example, in PRR, and then propagated to LIP to coordinate eye and arm movements. We show that, in our task, PRR reflects movement direction before LIP (Figure 7A). A dominant role for LIP in reaching is suggested by the fact that saccades usually precede reaches.[82] However, eye tracking methods (e.g., eye coils, video recording) are generally more sensitive to movement onset than arm-tracking methods (e.g., capacitive switches, touch screens). Furthermore, spikes in oculomotor nuclei precede eye movements by ~20 ms and spikes in M1 precede arm movements by ~150 ms.[80,81] Therefore, the order of neural activation for eye and arm movement execution may not necessarily correspond to behavioral measures of eye and arm movement onsets.

Behavioral studies with human and animal subjects also suggest that saccade and reach planning is processed in a parallel manner. Reach preparation enhances visual processing,[91,92] and saccades coupled with reaches are executed more quickly than singular saccades.[88] Reach preparation enhances visual processing,[91,92] and saccades coupled with reaches are executed more quickly than singular saccades.[88] Furthermore, saccades and reaches can be spatially decoupled, and when decoupled, attention can be allocated separately to each effector's target.[55–58]

Our main finding is that, during the planning period before a reach, inferred information flows primarily from PRR to LIP (Figure 2). If LIP was a command center for spatial information processing, then brain regions such as PRR would be consumers of that information and information would primarily flow from LIP to PRR. Instead, we find that information flow is bidirectional, with at least twice the flow from PRR to LIP compared to LIP to PRR. This finding supports the interpretation that PRR shares spatial information with LIP about the reach.[93] Our approach relies on identifying similarities in the signals contained within PRR and LIP and then asking whether one signal is likely to be driving the other. There is a long history of using Granger causality analysis for this purpose, asking whether the history of one signal can predict the current modulation of the second signal, after taking into account the history of the second signal.[94] Spectral Granger causality analysis is a variant thereof that operates in frequency space rather than in the time domain but follows similar principles.[69,95] To increase confidence in our results, we used a second independent method of assessing information flow: time-lagged spike-LFP coherence.[17] Action potentials (spikes) propagate information along axons. Spikes give rise to synaptic currents, which in turn give rise to dendritic currents. These currents are thought to produce much of the modulation of the LFP.[73,74] Spike-LFP interactions have an inherent directional asymmetry. Spikes in area X can directly evoke an LFP response in area Y (Figure 5A), but the reverse direction requires three steps: LFP in area Y reflects synaptic and dendritic currents that can drive spikes in area Y, these spikes can drive currents in area X, and these currents can drive spikes in area X (Figure 5B). This asymmetry means that coherence

between spikes in area X and LFP in area Y is more likely to reflect a causal influence from area X to area Y (a single step) rather than from area Y back to area X (three steps). We tested this idea by computing coherence between spikes in one area and LFP in another after time-shifting them by different amounts, and then asking whether peak coherence occurred when a lag was imposed on spikes relative to LFPs (consistent with a causal influence from the area in which the spikes were recorded to the area in which the LFP was recorded) or when a lead was imposed on spikes (consistent with either common input to both areas or information flow from the area in which the LFP was recorded to the area in which the spikes were recorded). Critically, we used a simulation to show that our methodology was sound (Figure 5D). Our results support that spikes in PRR drive LFP in LIP; peak coherence from PRR to LIP occurred when a lag of ~10 ms was imposed on spikes relative to the LFPs (Figure 5E, cyan). This is long compared to axonal propagation and synaptic conduction (a few milliseconds) but consistent with the average difference in response latencies for direct connections between cortical areas and with previous reports of the timing of activity across areas.[76–78] Peak coherence from LIP to PRR was negative, consistent with an indirect effect of PRR-to-LIP flow or common input. Taken together, the LFP-LFP spectral Granger causality, the spike-LFP coherence analyses, and the time-lagged spike-LFP coherence analysis provide high confidence for the conclusion that more information flows from PRR to LIP than from LIP to PRR.

An alternate interpretation of our results that preserves a dominant role of LIP in guiding reaches is that LIP sends spatial information to PRR early in the trial, shortly after the target first appears. In this view, the information flow that we observe during the planning period is merely feedback, perhaps used to ensure that PRR has received the correct information from LIP. We rule out this possibility by showing that in the first 300, 400, or 500 ms of the trial, information still flows predominantly from PRR to LIP, not from LIP to PRR (Figures 7 and S9).

In summary, we quantified functional connectivity between PRR and LIP using time-lagged spike-LFP coherence and spectral LFP-LFP Granger causality to investigate the functional organization of microcircuits in posterior parietal cortex. PRR and LIP encode plans for arm and eye movements, respectively, but LIP has also been implicated in high-level abstract spatial processing. We found that the pattern of causal influence between the two areas supports parallel processing streams with asymmetric interactions that likely support eye-hand coordination (Figure 1C).

Limitations of the study

A pitfall of correlation-based analyses is that communication may reflect common input from a third area rather than direct communication between areas. To minimize this possibility, we focused on the movement preparation period when no new stimuli were presented and no task-related actions were performed, either of which might drive robust activity that might then serve as common input into PRR and LIP. The time-lagged spike-LFP coherence analysis rules out common input as the main driver for flow from PRR to LIP (spikes in PRR and LFP in LIP; Figures 5 and 6). With common input, coherence would be maximized when a lead was imposed on the spikes relative to the LFPs (simulation

results, Figure 5D). Instead, peak coherence occurs when a lag is imposed on the spikes. The time-lagged spike-LFP coherence from LIP to PRR is consistent with an acausal influence from PRR to LIP information flow plus a small amount of either common input to both areas or flow from LIP to PRR (Figures 5B, 5C, and S10).

A second pitfall of this study is our implicit assumption that information flow, inferred by lagged coherence values, is monotonically related to the magnitude of that coherence. However, this interpretation assumes that the information being encoded and the efficiency of the encoding is similar for flow in the two different directions. Finally, our coherence approach captures only linear relationships between the activity of the two regions. More sophisticated mathematical techniques such as generalized linear models or transfer entropy could be used to capture additional nonlinear relationships.[96,97] An even better approach to identify information flow is to make use of perturbations. Stimulating individual neurons to inject information into the system is ideal but requires knowing how the information is encoded. The converse approach of blocking transmission is almost as good—for example, by identifying projecting fibers and silencing them using a pharmacological or optogenetic approach.[98]

STAR★METHODS

RESOURCE AVAILABILITY

Lead contact—Request for further information should be directed to the lead contact, Lawrence H. Snyder (larry@eye-hand.wustl.edu).

Materials availability—Not applicable. This study did not generate reagents.

Data and code availability

- Original data are available at https://doi.org/10.5281/zenodo.10811347.

- Original codes are available at https://doi.org/10.5281/zenodo.10811347.

- Any additional information required to reanalyze the data reported in this paper is available from the lead contact upon request.

EXPERIMENTAL MODEL AND SUBJECT DETAILS

Two male rhesus macaques (macaca mulatta), aged approximately 14 and 16 years were used for this study. All procedures conformed to the Guide for the Care and Use of Laboratory Animals and were approved by the Washington University Institutional Animal Care and Use Committee.

METHOD DETAILS

Apparatus—Experiments took place in a dark room. Head-fixed animals sat in a custom-designed monkey chair (Crist Instrument, Hagerstown, Maryland) with an open front to allow unimpaired reaching movements with both arms. Visual stimuli were back-projected by an LCD projector onto a translucent plexiglass screen mounted vertically ~40 cm in front of the animal. Eight target positions on the screen were organized in a rectangle centered on

the fixation point, each target ~8 cm (11°) or ~11 cm (15°) from the center fixation point. At each target location, a small piece of plexiglass (5 cm × 1 cm) oriented in the sagittal plane was mounted on the front of the projection screen to bisect the touching surface. The animals were trained to reach with the left and right hands to the left and right sides, respectively, of the plexiglass divider. Touches were monitored every 2 ms using 9 pairs of capacitive sensors. One pair of sensors served as home pads to detect reach starting points. Each of the remaining sensor pairs were placed behind a target position, one on each side of the plexiglass, to detect reach endpoints. Thus, for every target, each hand activated a unique capacitive sensor, even when both hands reached to the same target. Eye position was monitored using an infrared video eye-tracking system (120 Hz ISCAN eye-tracking laboratory, ETL-400).

Behavioral tasks—The task design and the movement conditions are shown in Figure 2. The animals performed delayed saccade-only movements or coordinated eye and arm movements with the left, right, or both arms. Animals first fixated on a circular white stimulus (1.5° × 1.5°) centered on the screen in front of them. Left and right hands touched home pads situated at waist height and 20 cm in front of each shoulder. After holding fixation (±5°) and initial arm positions for a fixed duration of 500 ms, either one or two peripheral targets (5° × 5°) appeared on the screen for 1250–1750 ms. Fixation was required throughout this instructed delay period. After the delay, the central eye fixation target shrank in size to a single pixel, cueing the animal to move to the peripheral target(s) in accordance with target color. A blue target instructed a reach with both arms ("bimanual-together"). A green or red target instructed a reach with the left or right arm, respectively. The simultaneous appearance of two targets (red and green) cued a reach with both arms to two different targets ("bimanual-apart"). Only trials in which the two targets were separated by 180° relative to the central fixation point are used for the current report (i.e., reaches to the left and right, top and bottom, or opposed diagonal locations). For bimanual-apart reaches, the arms could be uncrossed or crossed. Finally, a white target instructed a saccade without a reach. To help ensure as natural coordination as possible, animals were not trained to make arm movements without accompanying eye movements. All single-target reach trials require an accompanying saccade to the target. Saccades were optional (but almost always performed) for two-target reach trials.

All trial types were randomly interleaved within sets of 10 or 40 trials (one each per condition [5] and direction [2 or 8]). Throughout saccade and unimanual reach trials, hands not instructed to move were required to remain on their respective home buttons. On bimanual trials, the left and right hands were required to hit their target(s) within 500 ms of one another. Animals were required to maintain their hand(s) on the final target(s) for 300 ms. Spatial tolerance for saccades was ±5°. When an error occurred (a failure to achieve or maintain the required eye or hand positions), the trial was aborted, and short time-out ensued: 1500ms for an early fixation break and 500ms for a targeting error. Aborted trials were excluded from further analyses. Successful trials were rewarded with a drop of water or juice.

Electrophysiological recordings—Recordings were made from the left and right hemispheres of two adult male rhesus monkeys. In each animal, two recording chambers were centered at ~8 mm posterior to the ear canals and ~12 mm lateral of the midline on each side and placed flush to the skull. Anatomical magnetic resonance images were used to localize the medial bank of the intraparietal sulcus. Extracellular recordings were made using glass-coated tungsten electrodes (Alpha Omega, Alpharetta, GA; electrode impedance 0.5–3.0 MΩ at 1kHz) recorded from a steel guide tube in the same recording well. Neural signals were processed and saved using the Plexon MAP system (Plexon, Inc.). Signals were passed through a pre-amplifier and then separated into two signal paths. The LFP channel was band-pass filtered between 0.7 and 300 Hz and digitized at 1 kHz. We used a band-pass filter to remove 60 Hz power from the LFP. The spike channel was band-pass filtered between 100 Hz and 8 kHz and digitized at 25 kHz. Single units were isolated online via manually-set waveform triggers. During each recording session, one or two electrodes were placed in PRR and LIP in each hemisphere, up to a total of 4 electrodes. While searching for cells, animals performed saccade-only trials and combined reach plus saccade trials with the contralateral arm (contralateral with respect to the side of the isolated cell). Online, the preferred direction for a cell was defined as the target location that resulted in the largest sustained firing during the delay period. The null direction was defined as the diametrically opposite direction. Data were then collected for all trial types. As an indirect marker of inter-areal communication, we computed both inter-areal spike-LFP coherence and LFP-LFP spectral Granger causality over a broad range of frequencies.

Spike-LFP coherence—Coherence spectra between spikes in one area and LFP signals in another were computed over the last 800 ms before the go cue and from 50 to 550 ms after target onset. With fewer spikes, spike-LFP coherence is biased toward higher values and becomes increasingly unreliable. We included only those spike-LFP pairs with at least 500 spikes when combining over task types (Figures 2B, 2C, 7B, S4A, S4B, S8, and S9A) or 300 or 400 spikes when computing coherence separately for each task type (Figures 3A, 3B, 6, S5A, S5B, S6, S7A, and S7B). Key findings were confirmed using pairwise phase consistency, an alternative method of computing coherence that circumvents this bias.[67] We computed spike-LFP coherence using a multitaper method implemented in the Chronux toolbox (http://chronux.org/).[99] The number of tapers was typically 9 (but see next section).

Mean coherence spectra were estimated as follows. First, Fourier transforms were computed for each trial, n, and each taper, k, according to Equations 1 and 2 with t as the sample index, T as the number of samples per time series, f as the frequency in Hz, j as the imaginary unit (i.e., $\sqrt{-1}$), $d_k(t)$ as the taper time series for taper k, and $x_n(t)$ and $y_n(t)$ as the spike or LFP time series for trial n. For the spike time series, the DC component, i.e., the average value over time, was subtracted before transformation.

$$X_{n,k}(f) = \sum_{t=1}^{T} d_k(t)x_n(t)e^{-2\pi jft}$$

(Equation 1)

$$Y_{n,k}(f) = \sum_{t=1}^{T} d_k(t) y_n(t) e^{-2\pi jft}$$

(Equation 2)

The power spectral densities for a single trial, $S_{xx,n}(f)$ and $S_{yy,n}(f)$, were then computed as an average of the cross-spectra across K tapers according to Equations 3 and 4.

$$S_{xx,n}(f) = \frac{1}{f_s K} \sum_{k=1}^{K} |X_{n,k}(f)|^2$$

(Equation 3)

$$S_{yy,n}(f) = \frac{1}{f_s K} \sum_{k=1}^{K} |Y_{n,k}(f)|^2$$

(Equation 4)

f_s is the sampling frequency, and K is the number of tapers. The power spectral densities, $S_{xx}(f)$ and $S_{yy}(f)$, were then averaged across N trials to produce a single estimate of the power spectral density according to Equations 5 and 6.

$$S_{xx}(f) = \frac{1}{N} \sum_{n=1}^{N} S_{xx,n}(f)$$

(Equation 5)

$$S_{yy}(f) = \frac{1}{N} \sum_{n=1}^{N} S_{yy,n}(f)$$

(Equation 6)

Next, a mean cross power spectrum, $S_{xy}(f)$, was computed by averaging spectral estimates across K tapers and N trials as in Equations 7 and 8 where $Y_{n,k}^*(f)$ represents the complex conjugate of $Y_{n,k}(f)$.

$$S_{xy,n}(f) = \frac{1}{f_s K} \sum_{k=1}^{K} X_{n,k}(f) Y_{n,k}^*(f)$$

(Equation 7)

$$S_{xy}(f) = \frac{1}{N} \sum_{n=1}^{N} S_{xy,n}(f)$$

(Equation 8)

Coherence was computed by normalizing the cross spectrum by the geometric mean of the power spectra as in Equation 9. Finally, coherence was averaged across spike-LFP pairs; note that coherence and thus its average are complex valued.

$$C_{xy}(f) = \frac{S_{xy}(f)}{\sqrt{S_{xx}(f)S_{yy}(f)}}$$

(Equation 9)

Most figures show data from within-hemisphere connections for the 4 reaching tasks combined. Figures 5 and 6 use all 5 tasks. Individual task data are shown in Figure 3. Figures 2 and 6 show data for across-hemisphere connections in addition to within-hemisphere ones.

Time-lagged spike-LFP coherence analysis—To further investigate inter-areal signal flow, we asked if there is a clear lag or lead in spikes relative to LFP that maximizes spike-LFP coherence. A lag in spikes is consistent with direct communication (Figure 5A), and a lead is consistent with either communication in the reverse direction or common input (Figures 5B and 5C). We calculated coherence after imposing a lag or lead on the spikes with respect to the LFPs from −128 ms to +128 ms. We then asked, for a given LFP frequency, what lag or lead maximized coherence (peak shift). A representative example of the analysis centered at 25 Hz is shown in Figure 5E. We repeated this at 20 different logarithmically-spaced frequencies from 9 to 128 Hz. A pitfall of this analysis is that even if there is no shared information, there will always be some lag that produces maximum coherence. In that case, the peak shift would be equally likely to occur anywhere between −128 and +128 ms. For the main analysis (Figure 6), peak shifts were computed separately for each of the 5 tasks, using 23 tapers and a frequency half-bandwidth of 15 Hz. The data were then plotted only for those center frequencies in which the peak shifts for the 5 tasks were clustered. Statistically significant clustering was determined using a randomization test and a criterion value of $p < 0.001$.

Spike-LFP pairwise phase consistency (PPC)—The LFP phase at the time of each spike was estimated with a wavelet transform but was not pooled across trials. PPC was estimated according to Equation 10 (Figures S2).

$$PPC = \frac{1}{N(N-1)} \left(\left\| \sum_{n=1}^{N} \left(\frac{1}{S_n} \sum_{s=0}^{s_n} \exp(j\theta_{n,s}) \right) \right\|^2 - \sum_{n=1}^{N} \left\| \frac{1}{S_n} \sum_{s=0}^{s_n} \exp(j\theta_{n,s}) \right\|^2 \right)$$

(Equation 10)

N is the total number of trials, and S_n is the number of spikes in trial *n*, and $\theta_{n,s}$ is the phase at the time of spike *s* in trial *n*.

Spectral LFP-LFP Granger causality—We recorded 137 pairs of LFPs in PRR and LIP in the same hemisphere (56 and 81 pairs in each animal, respectively), and 137 pairs in different hemispheres (58 and 79 pairs in each animal, respectively). We used nonparametric bivariate spectral Granger causality to quantify causal relationships between these signal pairs using the FieldTrip toolbox.[64] Granger causality assays information flow from signal *x* to signal *y* by quantifying how much of the variance of signal *y* can be explained by the recent history of the two signals together compared to just the history of signal *y* alone.[94] If this difference is large, then signal *x* is presumed to causally influence signal *y*. Results from time-based autoregressive models, however, depend on the model order and may not fully take spectral characteristics of data into account.[100,101] To study frequency-specific causal interactions between LFP signals, we calculated spectral Granger causality $GC_{x \rightarrow y}(\omega)$ from a signal *x* to another signal *y* at frequency ω to estimate causal interactions using cross-spectral density matrix factorization according to Equations 11 and 12.[69,95]

$$GC_{x \rightarrow y}(\omega) = ln\left(\frac{S_{yy}(\omega)}{S_{yy}(\omega) - \left(\Sigma_{xx} - \frac{\Sigma_{xx}}{\Sigma_{yy}}|H_{yx}(\omega)|^2\right)}\right)$$

(Equation 11)

$$S(\omega) = H(\omega)\Sigma H(\omega)*$$

(Equation 12)

$S(\omega)$ and $H(\omega)$ are the cross-spectral density matrix and the spectral transfer matrix for a pair of signals at frequency ω, respectively. Σ is the covariance of an autoregressive model's residuals. Note that effects below 16 Hz were unreliable (Figure S3).

Statistics—All trial types were randomly interleaved for each cell or site in a recording session. Statistical analyses were performed in MATLAB (Mathworks) and R Statistical Software (version 4.2.0; The R Foundation for Statistical Computing). All statistical tests were two-sided unless specified otherwise. Chance levels of coherence and Granger causality were computed using permutation analysis (1000 and 200 repetitions, respectively). For spike-LFP coherence and PPC, spike times were randomized within each trial by permuting the interspike intervals. For Granger causality, LFP signals from each electrode in a pair were permuted across trials. Gray regions show the 1st to 99th percentiles of the permuted trials (Figures 2, 3, 7B, 7C, S2, S5, S7, S8, and S9); values above these gray regions are significant at the p < 0.01 (one-tailed) level. To test for significance between pairs of conditions (Figures 2, 7, S2A, S3, S4, S8, and S9), pooled t-tests or Wilcoxon signed-rank tests were applied at each frequency. Because Granger causality is a biased statistic with a minimum of 0 but no upper bound, we used Wilcoxon signed-rank tests for Granger causality values. Computing the appropriate multiple comparisons correction for the ~80 tests is difficult because data values at nearby frequencies are not independent,

and frequency smoothing in the analysis exacerbates these dependencies. We therefore set a conservative criterion of $p < 0.001$ at four or more contiguous frequency bands for spike-LFP, and $p < 0.001$ or $p < 0.01$ at four or more contiguous band for Granger causality, and at least one condition to be outside of the 1st and 99th percentile bounds of the permutation tests.

Modeling—To establish and confirm our theoretical predictions regarding spike-LFP coherence, we built a model linking spikes and LFP. Spikes are action potentials that travel along the axon. LFP is believed to primarily reflect the movement of charge in the dendrites and soma.[73] A complete model requires knowing how incoming spikes drive the post-synaptic flow of charge, and how this charge then drives outgoing spikes. Rather than record intracellularly, we use extracellular local field potentials as a correlate of the flow of charge. To be clear, the LFP itself has little or no direct causal role in driving outgoing spikes; it is instead a generally accepted surrogate for the involved processes. Unfortunately, we lack a full understanding of how intracellular charge flow relates to LFP signals, what other LFP drivers exist and how those drivers behave. We can estimate the LFP response to incoming spikes, essentially the spike-to-LFP transfer function, using electrical micro-stimulation. Optogenetic stimulation is non-optimal because it drives artifactual LFP signals.[102] Electrical stimulation also produces artifacts, but they are transient and can be filtered out. Action potentials can be evoked using local stimulation to estimate effects on LFP, and, in particular, on beta band oscillations. While the details depend on the phase of on-going beta at the time of stimulation, 1–2 pulses (0.1 ms, 80 μA, interstimulus interval 25–120 ms) reliably increase beta oscillation amplitude with a latency of ~10 ms and a peak effect at ~40 ms.[103] Trains of up to 8 pulses were used in this particular study, but no more than 2 pulses preceded the time of peak effect. For a coarse estimate of the spiking response to LFP, that is, the LFP-to-spike transfer function, we can look at a spike-triggered average of LFP. LFP activity is modulated both before and after spikes.[104,105] LFP modulation after a spike likely reflects both driving and driven processes. LFP modulation before the spike would capture the LFP correlates of the signal that drives that spike. However, this modulation could also include LFP signals driven by spikes from nearby cells that are correlated with and precede (but do not drive) the index spike. Thus, our current findings confirm that spikes do appear to drive LFP oscillations, particularly in the beta band, and that LFP modulation reliably precedes spike initiation, but at this time we can only approximate the precise relationships.

With these limitations in mind, we built a chain of activity consisting of 4 serially-connected neurons. Action potentials from one cell produces an LFP response, modeled as a short burst of beta frequency, and the resulting LFP responses are used to predict how the underlying current flow evokes spikes in the next neuron in the chain. Using 2–5 neurons gave similar results as 4, leading to identical conclusions. We begin with actual LFP signals recorded from PRR. To convert LFP signals to spikes, we convolve the LFP signal with a matched filter to detect instances of 1–6 cycles of (windowed) 20–40 Hz oscillation that occur within the full-spectrum LFP signal (0–240 Hz). We then threshold the output of the matched filter to produce a binary output (1's or 0's) representing a spike train. The threshold was adjusted to produce a desired firing rate, from 10 to 240 Hz. We add stochasticity by adding from

50 to 200% more (random) Poisson-distributed spikes to the thresholded output. To convert spike trains into an LFP signal, we convolve them with the same matched filter and add the output to an actual LFP signal recorded from PRR. Critically, we built in pure time-delays for spike generation (the time between LFP and spikes, which we set at 2 ms) and for axonal conduction and synaptic delays (the time between spikes and LFP, which we set at 6 ms). We varied these values from 1 to 30 ms, with the latter always larger than the former. We tested extensively and found that all parameter values led to qualitatively similar conclusions (see below).

To use this model to generate the predictions of Figure 5, we computed coherence values between spikes and LFP in the model neurons. As in the actual data analysis, spikes were shifted in time, relative to the LFP, by values from 0 to ±200 ms. We did not zero-pad or rotate the data; instead, we computed coherence within a window that is smaller than our original data length. This meant that a forward shift of, for example, 100 ms would effectively slide our spike window within the original data stream, while keeping the time of the LFP window constant. In the actual data analysis, we eliminated spikes rather than shifting them, since shifting spikes would risk introducing early, stimulus-evoked spikes, or late, movement-related spikes into our analysis, thereby biasing the results. Doing this in the model produces similar results. Windows from 50 to 5000 ms gave similar results. Coherence was computed using the R "seewave" package to avoid any potential artifacts from our own coherence code (which is MATLAB-based and uses the Chronux toolbox[99]; an in-house wavelet-based method gives similar results).

To generate predictions for lagged spike-LFP coherence profiles from spikes in a source area and LFP in a receiving area (Figure 5A), we computed coherence between spikes from the first neuron in our chain and LFP from the last neuron. Here we show coherence at 25 ± 2 Hz, though nearby bands gave similar results. We simulated having data from 7 different paired recording sites and 10–1200 trials from each site (Figure 5D). To predict lagged spike-LFP coherence profiles from spikes in a receiving area and LFP in a source area (Figure 5B), we computed coherence between spikes from the last neuron and LFP from the first neuron. To predict lagged spike-LFP coherence profiles resulting from common input (Figure 5C), we modified the model so that each cell was driven by the same LFP input, and computed coherence between either spikes of the first neuron and LFP of the last, or vice versa. Note that the addition of noise in the spike generation (see above) ensured that the actual spike trains from each cell were unique, and the addition of different LFP signals to each LFP (see above) ensured that, even in the absence of the spike generation noise, each LFP would be unique.

We saw clear effects of time shifts under causal (Figure 5A) as well as acausal (Figure 5B) conditions. In the causal case, coherence is maximized when a lag is imposed on the spikes that is approximately equal to the sum of the pure delays (blue line of Figure 5D). In the acausal direction (orange), coherence is maximized by a lead of similar magnitude. In this case, however, the effect of the time shift was less robust than in the causal direction. Common input resulted in identical effects for the two directions, with a peak coherence within a few milliseconds of zero (purple). Changing model parameters scaled the curves on either the *x* or *y* axis. For example, decreasing the time window in which coherence

was computed or increasing the number of trials produced narrower response functions. Including more stochastic noise or using a shorter matched filter lowered the responses. However, information flow from the site of spike recording to the site of LFP recording (causal information flow) always resulted in a peak coherence with a positive imposed lag, common input always resulted in a peak lag very close to zero (±3 ms) and acausal flow always resulted in a negative peak lag. The peak heights always fell in the same order (causal > common input > acausal) for any set of parameters. With large amounts of stochasticity, the curves, especially the acausal curve, could nearly disappear.

Figure 5D shows predictions for pure conditions. The positive peak for coherence that was actually observed between PRR spikes and LIP LFP (Figure 6A) is consistent with flow from PRR to LIP. The negative peak for coherence that was observed with the reverse configuration (Figure 6B) is qualitatively consistent with that same flow, that is, from PRR to LIP. However, we would have predicted an equal and opposite time shift; the observed negative peak shift for LIP-to-PRR is only about half as large as the observed positive peak shift from PRR to LIP. In addition, we suspected from the zero-lag coherence analysis that there was some degree of flow from LIP to PRR (Figure 2B), yet there is no positive peak in coherence from LIP to PRR. To address these points, we constructed predictions for combined information flows using linear superposition. This has many limitations but is good for a first-pass consideration. Figure S10A shows the predicted lagged spike-LFP coherence for a mixture of flow from PRR to LIP, plus a flow from LIP to PRR that is half as strong. The results are quite different from the observed data (Figure S10D). In order to match the observed results – a peak in LIP-to-PRR coherence at a negative lag time plus a coherence amplitude ratio of about two to one, the information flow from LIP to PRR cannot be more that about 20% of the flow from PRR to LIP (Figures S10E and S10F).

We have shown that computing the coherence between two signals is a useful way to assay shared information. It is not immediately transparent why this method should work. Certainly it is appropriate to consider coherence analysis for spike-LFP interactions where we have reason to believe that an action potential will result in the addition of a small flutter (an oscillatory signal of limited bandwidth) to the LFP. Because it operates in the frequency domain rather than the time domain, coherence compares only the frequency spectra of the two signals without regard to the timing of individual events within each series. This theory-based description would be realized if one had infinite data. In that case, shifting one signal with respect to the other, that is, changing the relative timing between the two signals, would have no effect on coherence magnitude. As a result, with infinitely long trials, plots of coherence versus imposed lag on spikes (Figures 5D and 5E) would be flat lines. However, trials are not infinite in length. In addition, trials must be further subdivided by windowing (e.g., tapers) in order to compute coherence. In the case of events that occur simultaneously in the two signals, shifting one signal in time with respect to the other may move some corresponding events (e.g., an action potential in one signal and a corresponding LFP event in the other) into different windows. This will lower signal coherence. If the events are not precisely aligned in time to start with, then the shift may either increase or decrease coherence, depending on whether the shift brings the corresponding events closer into alignment with each other or moves them farther apart from each other.

We conclude that the lagged spike-LFP coherence is a potentially useful way of ascertaining causal effects between neurons. The peak lag (the lag imposed on spikes that produces the maximum coherence) is related to the direction of information flow. Positive peaks are consistent with a flow from the site at which spikes are recorded to the site at which LFP is recorded. Negative peaks are consistent with the reverse flow. Peak lags close to zero are consistent with common input.

Supplementary Material

Refer to Web version on PubMed Central for supplementary material.

ACKNOWLEDGMENTS

REFERENCES

1. Blank SC, Scott SK, Murphy K, Warburton E, and Wise RJS (2002). Speech production: Wernicke, Broca and beyond. Brain 125, 1829–1838. 10.1093/brain/awf191. [PubMed: 12135973]

2. Norman SL, Maresca D, Christopoulos VN, Griggs WS, Demene C, Tanter M, Shapiro MG, and Andersen RA (2021). Single-trial decoding of movement intentions using functional ultrasound neuroimaging. Neuron 109, 1554–1566.e4. 10.1016/j.neuron.2021.03.003. [PubMed: 33756104]

3. Paninski L, Pillow J, and Lewi J (2007). Statistical models for neural encoding, decoding, and optimal stimulus design. In Progress in Brain Research (Elsevier), pp. 493–507. 10.1016/S0079-6123(06)65031-0.

4. Lomber SG (1999). The advantages and limitations of permanent or reversible deactivation techniques in the assessment of neural function. J. Neurosci. Methods 86, 109–117. 10.1016/S0165-0270(98)00160-5. [PubMed: 10065980]

5. Zhou Y, and Freedman DJ (2019). Posterior parietal cortex plays a causal role in perceptual and categorical decisions. Science 365, 180–185. 10.1126/science.aaw8347. [PubMed: 31296771]

6. Donahue CJ, Sotiropoulos SN, Jbabdi S, Hernandez-Fernandez M, Behrens TE, Dyrby TB, Coalson T, Kennedy H, Knoblauch K, Van Essen DC, and Glasser MF (2016). Using Diffusion Tractography to Predict Cortical Connection Strength and Distance: A Quantitative Comparison with Tracers in the Monkey. J. Neurosci 36, 6758–6770. 10.1523/JNEUROSCI.0493-16.2016. [PubMed: 27335406]

7. Lewis JW, and Van Essen DC (2000). Corticocortical connections of visual, sensorimotor, and multimodal processing areas in the parietal lobe of the macaque monkey. J. Comp. Neurol 428, 112–137. 10.1002/1096-9861(20001204)428:1<112::AID-CNE8>3.0.CO;2-9. [PubMed: 11058227]

8. Lipski J (1981). Antidromic activation of neurones as an analytic tool in the study of the central nervous system. J. Neurosci. Methods 4, 1–32. 10.1016/0165-0270(81)90015-7. [PubMed: 7253697]

9. Moore T, and Armstrong KM (2003). Selective gating of visual signals by microstimulation of frontal cortex. Nature 421, 370–373. 10.1038/nature01341. [PubMed: 12540901]

10. Power JD, Cohen AL, Nelson SM, Wig GS, Barnes KA, Church JA, Vogel AC, Laumann TO, Miezin FM, Schlaggar BL, and Petersen SE (2011). Functional Network Organization of the Human Brain. Neuron 72, 665–678. 10.1016/j.neuron.2011.09.006. [PubMed: 22099467]

11. Felleman DJ, and Van Essen DC (1991). Distributed hierarchical processing in the primate cerebral cortex. Cerebr. Cortex 1, 1–47. 10.1093/cercor/1.1.1-a.

12. Bode S, and Haynes J-D (2009). Decoding sequential stages of task preparation in the human brain. Neuroimage 45, 606–613. 10.1016/j.neuroimage.2008.11.031. [PubMed: 19111624]

13. Ferrier J, Tiran E, Deffieux T, Tanter M, and Lenkei Z (2020). Functional imaging evidence for task-induced deactivation and disconnection of a major default mode network hub in the mouse brain. Proc. Natl. Acad. Sci. USA 117, 15270–15280. 10.1073/pnas.1920475117. [PubMed: 32541017]

14. Sun FT, Miller LM, Rao AA, and D'Esposito M (2007). Functional Connectivity of Cortical Networks Involved in Bimanual Motor Sequence Learning. Cerebr. Cortex 17, 1227–1234. 10.1093/cercor/bhl033.

15. Bernasconi C, and König P (1999). On the directionality of cortical interactions studied by structural analysis of electrophysiological recordings. Biol. Cybern 81, 199–210. 10.1007/s004220050556. [PubMed: 10473845]

16. Brovelli A, Ding M, Ledberg A, Chen Y, Nakamura R, and Bressler SL (2004). Beta oscillations in a large-scale sensorimotor cortical network: Directional influences revealed by Granger causality. Proc. Natl. Acad. Sci. USA 101, 9849–9854. 10.1073/pnas.0308538101. [PubMed: 15210971]

17. Schneider M, Broggini AC, Dann B, Tzanou A, Uran C, Sheshadri S, Scherberger H, and Vinck M (2021). A mechanism for inter-areal coherence through communication based on connectivity and oscillatory power. Neuron 109, 4050–4067.e12. 10.1016/j.neuron.2021.09.037. [PubMed: 34637706]

18. Baumann MA, Fluet M-C, and Scherberger H (2009). Context-Specific Grasp Movement Representation in the Macaque Anterior Intraparietal Area. J. Neurosci 29, 6436–6448. 10.1523/JNEUR-OSCI.5479-08.2009. [PubMed: 19458215]

19. Lanzilotto M, Ferroni CG, Livi A, Gerbella M, Maranesi M, Borra E, Passarelli L, Gamberini M, Fogassi L, Bonini L, and Orban GA (2019). Anterior Intraparietal Area: A Hub in the Observed Manipulative Action Network. Cerebr. Cortex 29, 1816–1833. 10.1093/cercor/bhz011.

20. Murata A, Gallese V, Luppino G, Kaseda M, and Sakata H (2000). Selectivity for the Shape, Size, and Orientation of Objects for Grasping in Neurons of Monkey Parietal Area AIP. J. Neurophysiol 83, 2580–2601. 10.1152/jn.2000.83.5.2580. [PubMed: 10805659]

21. Ilg UJ, and Thier P (2003). Visual Tracking Neurons in Primate Area MST Are Activated by Smooth-Pursuit Eye Movements of an "Imaginary" Target. J. Neurophysiol 90, 1489–1502. 10.1152/jn.00272.2003. [PubMed: 12736240]

22. Komatsu H, and Wurtz RH (1988). Relation of cortical areas MT and MST to pursuit eye movements. I. Localization and visual properties of neurons. J. Neurophysiol 60, 580–603. 10.1152/jn.1988.60.2.580. [PubMed: 3171643]

23. Scherberger H, Jarvis MR, and Andersen RA (2005). Cortical Local Field Potential Encodes Movement Intentions in the Posterior Parietal Cortex. Neuron 46, 347–354. 10.1016/j.neuron.2005.03.004. [PubMed: 15848811]

24. Snyder LH, Batista AP, and Andersen RA (1997). Coding of intention in the posterior parietal cortex. Nature 386, 167–170. 10.1038/386167a0. [PubMed: 9062187]

25. Barash S, Bracewell RM, Fogassi L, Gnadt JW, and Andersen RA (1991). Saccade-related activity in the lateral intraparietal area. I. Temporal properties; comparison with area 7a. J. Neurophysiol 66, 1095–1108. 10.1152/jn.1991.66.3.1095. [PubMed: 1753276]

26. Andersen RA, Brotchie PR, and Mazzoni P (1992). Evidence for the lateral intraparietal area as the parietal eye field. Curr. Opin. Neurobiol 2, 840–846. 10.1016/0959-4388(92)90143-9. [PubMed: 1477549]

27. Christopoulos VN, Bonaiuto J, Kagan I, and Andersen RA (2015). Inactivation of Parietal Reach Region Affects Reaching But Not Saccade Choices in Internally Guided Decisions. J. Neurosci 35, 11719–11728. 10.1523/JNEUROSCI.1068-15.2015. [PubMed: 26290248]

28. Brunamonti E, and Paré M (2023). Neuronal activity in posterior parietal cortex area LIP is not sufficient for saccadic eye movement production. Front. Integr. Neuroscience (San Diego, CA, U.S.) 17, 1251431. 10.3389/fnint.2023.1251431.

29. Gottlieb JP, Kusunoki M, and Goldberg ME (1998). The representation of visual salience in monkey parietal cortex. Nature 391, 481–484. 10.1038/35135. [PubMed: 9461214]

30. Platt ML, and Glimcher PW (1999). Neural correlates of decision variables in parietal cortex. Nature 400, 233–238. 10.1038/22268. [PubMed: 10421364]

31. Bisley JW, and Goldberg ME (2003). Neuronal Activity in the Lateral Intraparietal Area and Spatial Attention. Science 299, 81–86. 10.1126/science.1077395. [PubMed: 12511644]

32. Sugrue LP, Corrado GS, and Newsome WT (2004). Matching Behavior and the Representation of Value in the Parietal Cortex. Science 304, 1782–1787. 10.1126/science.1094765. [PubMed: 15205529]

33. Sereno AB, and Amador SC (2006). Attention and Memory-Related Responses of Neurons in the Lateral Intraparietal Area During Spatial and Shape-Delayed Match-to-Sample Tasks. J. Neurophysiol 95, 1078–1098. 10.1152/jn.00431.2005. [PubMed: 16221750]

34. Herrington TM, and Assad JA (2010). Temporal Sequence of Attentional Modulation in the Lateral Intraparietal Area and Middle Temporal Area during Rapid Covert Shifts of Attention. J. Neurosci 30, 3287–3296. 10.1523/JNEUROSCI.6025-09.2010. [PubMed: 20203188]

35. Kubanek J, and Snyder LH (2015). Reward-Based Decision Signals in Parietal Cortex Are Partially Embodied. J. Neurosci 35, 4869–4881. 10.1523/JNEUROSCI.4618-14.2015. [PubMed: 25810518]

36. Foley NC, Kelly SP, Mhatre H, Lopes M, and Gottlieb J (2017). Parietal neurons encode expected gains in instrumental information. Proc. Natl. Acad. Sci. USA 114, E3315–E3323. 10.1073/pnas.1613844114. [PubMed: 28373569]

37. Fiebelkorn IC, Pinsk MA, and Kastner S (2018). A Dynamic Interplay within the Frontoparietal Network Underlies Rhythmic Spatial Attention. Neuron 99, 842–853.e8. 10.1016/j.neuron.2018.07.038. [PubMed: 30138590]

38. Oristaglio J, Schneider DM, Balan PF, and Gottlieb J (2006). Integration of Visuospatial and Effector Information during Symbolically Cued Limb Movements in Monkey Lateral Intraparietal Area. J. Neurosci 26, 8310–8319. 10.1523/JNEUROSCI.1779-06.2006. [PubMed: 16899726]

39. de Lafuente V, Jazayeri M, and Shadlen MN (2015). Representation of Accumulating Evidence for a Decision in Two Parietal Areas. J. Neurosci 35, 4306–4318. 10.1523/JNEUROSCI.2451-14.2015. [PubMed: 25762677]

40. Gottlieb J (2007). From Thought to Action: The Parietal Cortex as a Bridge between Perception, Action, and Cognition. Neuron 53, 9–16. 10.1016/j.neuron.2006.12.009. [PubMed: 17196526]

41. Baizer JS, Ungerleider LG, and Desimone R (1991). Organization of visual inputs to the inferior temporal and posterior parietal cortex in macaques. J. Neurosci 11, 168–190. 10.1523/JNEUROSCI.11-01-00168.1991. [PubMed: 1702462]

42. Blatt GJ, Andersen RA, and Stoner GR (1990). Visual receptive field organization and cortico-cortical connections of the lateral intraparietal area (area LIP) in the macaque. J. Comp. Neurol 299, 421–445. 10.1002/cne.902990404. [PubMed: 2243159]

43. Yttri EA, Liu Y, and Snyder LH (2013). Lesions of cortical area LIP affect reach onset only when the reach is accompanied by a saccade, revealing an active eye-hand coordination circuit. Proc. Natl. Acad. Sci. USA 110, 2371–2376. 10.1073/pnas.1220508110. [PubMed: 23341626]

44. Yttri EA, Wang C, Liu Y, and Snyder LH (2014). The parietal reach region is limb specific and not involved in eye-hand coordination. J. Neurophysiol 111, 520–532. 10.1152/jn.00058.2013. [PubMed: 24198328]

45. Mooshagian E, Wang C, Holmes CD, and Snyder LH (2018). Single Units in the Posterior Parietal Cortex Encode Patterns of Bimanual Coordination. Cerebr. Cortex 28, 1549–1567. 10.1093/cercor/bhx052.

46. Mooshagian E, Holmes CD, and Snyder LH (2021). Local field potentials in the parietal reach region reveal mechanisms of bimanual coordination. Nat. Commun 12, 2514. 10.1038/s41467-021-22701-3. [PubMed: 33947840]

47. Mooshagian E, Yttri EA, Loewy AD, and Snyder LH (2022). Contralateral Limb Specificity for Movement Preparation in the Parietal Reach Region. J. Neurosci 42, 1692–1701. 10.1523/JNEURO-SCI.0232-21.2021. [PubMed: 34996817]

48. Cui H, and Andersen RA (2007). Posterior Parietal Cortex Encodes Autonomously Selected Motor Plans. Neuron 56, 552–559. 10.1016/j.neuron.2007.09.031. [PubMed: 17988637]

49. Hwang EJ, Hauschild M, Wilke M, and Andersen RA (2012). Inactivation of the Parietal Reach Region Causes Optic Ataxia, Impairing Reaches but Not Saccades. Neuron 76, 1021–1029. 10.1016/j.neuron.2012.10.030. [PubMed: 23217749]

50. Liu Y, Yttri EA, and Snyder LH (2010). Intention and attention: different functional roles for LIPd and LIPv. Nat. Neurosci 13, 495–500. 10.1038/nn.2496. [PubMed: 20190746]

51. Hayhoe MM, Shrivastava A, Mruczek R, and Pelz JB (2003). Visual memory and motor planning in a natural task. J. Vis 3, 49–63. 10.1167/3.1.6. [PubMed: 12678625]

52. Rizzolatti G, Riggio L, Dascola I, and Umiltá C (1987). Reorienting attention across the horizontal and vertical meridians: Evidence in favor of a premotor theory of attention. Neuropsychologia 25, 31–40. 10.1016/0028-3932(87)90041-8. [PubMed: 3574648]

53. Corbetta M, and Shulman GL (2002). Control of goal-directed and stimulus-driven attention in the brain. Nat. Rev. Neurosci 3, 201–215. 10.1038/nrn755. [PubMed: 11994752]

54. Schall JD (2004). On the role of frontal eye field in guiding attention and saccades. Vis. Res 44, 1453–1467. 10.1016/j.visres.2003.10.025. [PubMed: 15066404]

55. Jonikaitis D, and Deubel H (2011). Independent Allocation of Attention to Eye and Hand Targets in Coordinated Eye-Hand Movements. Psychol. Sci 22, 339–347. 10.1177/0956797610397666. [PubMed: 21270450]

56. Kreyenmeier P, Deubel H, and Hanning NM (2020). Theory of visual attention (TVA) in action: Assessing premotor attention in simultaneous eye-hand movements. Cortex 133, 133–148. 10.1016/j.cortex.2020.09.020. [PubMed: 33120191]

57. Stewart EEM, and Ma-Wyatt A (2017). The profile of attention differs between locations orthogonal to and in line with reach direction. Atten. Percept. Psychophys 79, 2412–2423. 10.3758/s13414-017-1400-z. [PubMed: 28785967]

58. Nissens T, and Fiehler K (2018). Saccades and reaches curve away from the other effector's target in simultaneous eye and hand movements. J. Neurophysiol 119, 118–123. 10.1152/jn.00618.2017. [PubMed: 29021392]

59. Battaglia-Mayer A, Ferraina S, Genovesio A, Marconi B, Squatrito S, Molinari M, Lacquaniti F, and Caminiti R (2001). Eye-Hand Coordination during Reaching. II. An Analysis of the Relationships between Visuomanual Signals in Parietal Cortex and Parieto-frontal Association Projections. Cerebr. Cortex 11, 528–544. 10.1093/cercor/11.6.528.

60. Dean HL, Hagan MA, and Pesaran B (2012). Only Coherent Spiking in Posterior Parietal Cortex Coordinates Looking and Reaching. Neuron 73, 829–841. 10.1016/j.neuron.2011.12.035. [PubMed: 22365554]

61. Van Donkelaar P, Lee J-H, and Drew AS (2000). Transcranial Magnetic Stimulation Disrupts Eye-Hand Interactions in the Posterior Parietal Cortex. J. Neurophysiol 84, 1677–1680. 10.1152/jn.2000.84.3.1677. [PubMed: 10980038]

62. Mooshagian E, and Snyder LH (2018). Spatial eye–hand coordination during bimanual reaching is not systematically coded in either LIP or PRR. Proc. Natl. Acad. Sci. USA 115, E3817–E3826. 10.1073/pnas.1718267115. [PubMed: 29610356]

63. Khazali MF, Wong YT, Dean HL, Hagan MA, Fabiszak MM, and Pesaran B (2023). Putative cell-type-specific multiregional mode in posterior parietal cortex during coordinated visual behavior. Neuron 111, 1979–1992.e7. 10.1016/j.neuron.2023.03.023. [PubMed: 37044088]

64. Oostenveld R, Fries P, Maris E, and Schoffelen J-M (2011). Field-Trip: Open Source Software for Advanced Analysis of MEG, EEG, and Invasive Electrophysiological Data. Comput. Intell. Neurosci 2011, 156869–9. 10.1155/2011/156869. [PubMed: 21253357]

65. Chen Y, Bressler SL, and Ding M (2006). Frequency decomposition of conditional Granger causality and application to multivariate neural field potential data. J. Neurosci. Methods 150, 228–237. 10.1016/j.jneumeth.2005.06.011. [PubMed: 16099512]

66. Khanna P, and Carmena JM (2015). Neural oscillations: beta band activity across motor networks. Curr. Opin. Neurobiol 32, 60–67. 10.1016/j.conb.2014.11.010. [PubMed: 25528615]

67. Vinck M, Battaglia FP, Womelsdorf T, and Pennartz C (2012). Improved measures of phase-coupling between spikes and the Local Field Potential. J. Comput. Neurosci 33, 53–75. 10.1007/s10827-011-0374-4. [PubMed: 22187161]

68. Hacking I. (1983). Representing and Intervening: Introductory Topics in the Philosophy of Natural Science (Cambridge University Press).

69. Bastos AM, and Schoffelen J-M (2015). A Tutorial Review of Functional Connectivity Analysis Methods and Their Interpretational Pitfalls. Front. Syst. Neurosci 9, 175. 10.3389/fnsys.2015.00175. [PubMed: 26778976]

70. Haufe S, Nikulin VV, and Nolte G (2012). Alleviating the Influence of Weak Data Asymmetries on Granger-Causal Analyses. In Latent Variable Analysis and Signal Separation Lecture Notes in Computer Science, Theis F, Cichocki A, Yeredor A, and Zibulevsky M, eds. (Springer Berlin Heidelberg), pp. 25–33. 10.1007/978-3-642-28551-6_4.

71. Vinck M, Huurdeman L, Bosman CA, Fries P, Battaglia FP, Pennartz CMA, and Tiesinga PH (2015). How to detect the Granger-causal flow direction in the presence of additive noise? Neuroimage 108, 301–318. 10.1016/j.neuroimage.2014.12.017. [PubMed: 25514516]

72. Mooshagian E, Wang C, Ferdoash A, and Snyder LH (2014). Movement order and saccade direction affect a common measure of eye-hand coordination in bimanual reaching. J. Neurophysiol 112, 730–739. 10.1152/jn.00234.2014. [PubMed: 24848462]

73. Buzsáki G, Anastassiou CA, and Koch C (2012). The origin of extracellular fields and currents — EEG, ECoG, LFP and spikes. Nat. Rev. Neurosci 13, 407–420. 10.1038/nrn3241. [PubMed: 22595786]

74. Einevoll GT, Kayser C, Logothetis NK, and Panzeri S (2013). Modelling and analysis of local field potentials for studying the function of cortical circuits. Nat. Rev. Neurosci 14, 770–785. 10.1038/nrn3599. [PubMed: 24135696]

75. Bastos AM, Vezoli J, and Fries P (2015). Communication through coherence with inter-areal delays. Curr. Opin. Neurobiol 31, 173–180. 10.1016/j.conb.2014.11.001. [PubMed: 25460074]

76. Schmolesky MT, Wang Y, Hanes DP, Thompson KG, Leutgeb S, Schall JD, and Leventhal AG (1998). Signal Timing Across the Macaque Visual System. J. Neurophysiol 79, 3272–3278. 10.1152/jn.1998.79.6.3272. [PubMed: 9636126]

77. Gregoriou GG, Gotts SJ, Zhou H, and Desimone R (2009). High-Frequency, Long-Range Coupling Between Prefrontal and Visual Cortex During Attention. Science 324, 1207–1210. 10.1126/science.1171402. [PubMed: 19478185]

78. Baldauf D, and Desimone R (2014). Neural Mechanisms of Object-Based Attention. Science 344, 424–427. 10.1126/science.1247003. [PubMed: 24763592]

79. Biguer B, Jeannerod M, and Prablanc C (1982). The coordination of eye, head, and arm movements during reaching at a single visual target. Exp. Brain Res 46, 301–304. 10.1007/BF00237188. [PubMed: 7095037]

80. Fuchs AF, and Luschei ES (1970). Firing patterns of abducens neurons of alert monkeys in relationship to horizontal eye movement. J. Neurophysiol 33, 382–392. 10.1152/jn.1970.33.3.382. [PubMed: 4985724]

81. Georgopoulos AP, Kalaska JF, Caminiti R, and Massey JT (1982). On the relations between the direction of two-dimensional arm movements and cell discharge in primate motor cortex. J. Neurosci 2, 1527–1537. 10.1523/JNEUROSCI.02-11-01527.1982. [PubMed: 7143039]

82. Kubanek J, Wang C, and Snyder LH (2013). Neuronal responses to target onset in oculomotor and somatomotor parietal circuits differ markedly in a choice task. J. Neurophysiol 110, 2247–2256. 10.1152/jn.00968.2012. [PubMed: 23966670]

83. Sheliga BM, Riggio L, and Rizzolatti G (1994). Orienting of attention and eye movements. Exp. Brain Res 98, 507–522. 10.1007/BF00233988. [PubMed: 8056071]

84. Carrasco M, and McElree B (2001). Covert attention accelerates the rate of visual information processing. Proc. Natl. Acad. Sci. USA 98, 5363–5367. 10.1073/pnas.081074098. [PubMed: 11309485]

85. Dean HL, Martí D, Tsui E, Rinzel J, and Pesaran B (2011). Reaction Time Correlations during Eye-Hand Coordination: Behavior and Modeling. J. Neurosci 31, 2399–2412. 10.1523/JNEUROSCI.4591-10.2011. [PubMed: 21325507]

86. Prablanc C, Echallier JE, Jeannerod M, and Komilis E (1979). Optimal response of eye and hand motor systems in pointing at a visual target. Biol. Cybern 35, 183–187. [PubMed: 518938]

87. Rogal L, Reible G, and Fischer B (1985). Reaction times of the eye and the hand of the monkey in a visual reach task. Neurosci. Lett 58, 127–132. 10.1016/0304-3940(85)90341-6. [PubMed: 4047471]

88. Snyder LH, Calton JL, Dickinson AR, and Lawrence BM (2002). Eye-Hand Coordination: Saccades Are Faster When Accompanied by a Coordinated Arm Movement. J. Neurophysiol 87, 2279–2286. 10.1152/jn.00854.2001. [PubMed: 11976367]

89. Hagan MA, Dean HL, and Pesaran B (2012). Spike-field activity in parietal area LIP during coordinated reach and saccade movements. J. Neurophysiol 107, 1275–1290. 10.1152/jn.00867.2011. [PubMed: 22157119]

90. Wong YT, Fabiszak MM, Novikov Y, Daw ND, and Pesaran B (2016). Coherent neuronal ensembles are rapidly recruited when making a look-reach decision. Nat. Neurosci 19, 327–334. 10.1038/nn.4210. [PubMed: 26752158]

91. Perry CJ, and Fallah M (2017). Effector-based attention systems: Effector-based attention. Ann. N. Y. Acad. Sci 1396, 56–69. 10.1111/nyas.13354. [PubMed: 28548458]

92. Rolfs M, Lawrence BM, and Carrasco M (2013). Reach preparation enhances visual performance and appearance. Philos. Trans. R. Soc. Lond. B Biol. Sci 368, 20130057. 10.1098/rstb.2013.0057. [PubMed: 24018719]

93. Hwang EJ, Hauschild M, Wilke M, and Andersen RA (2014). Spatial and Temporal Eye-Hand Coordination Relies on the Parietal Reach Region. J. Neurosci 34, 12884–12892. 10.1523/JNEURO-SCI.3719-13.2014. [PubMed: 25232123]

94. Barnett L, and Seth AK (2014). The MVGC multivariate Granger causality toolbox: A new approach to Granger-causal inference. J. Neurosci. Methods 223, 50–68. 10.1016/j.jneumeth.2013.10.018. [PubMed: 24200508]

95. Geweke J (1982). Measurement of Linear Dependence and Feedback between Multiple Time Series. J. Am. Stat. Assoc 77, 304–313. 10.1080/01621459.1982.10477803.

96. Vicente R, Wibral M, Lindner M, and Pipa G (2011). Transfer entropy—a model-free measure of effective connectivity for the neurosciences. J. Comput. Neurosci 30, 45–67. 10.1007/s10827-010-0262-3. [PubMed: 20706781]

97. Yates JL, Park IM, Katz LN, Pillow JW, and Huk AC (2017). Functional dissection of signal and noise in MT and LIP during decision-making. Nat. Neurosci 20, 1285–1292. 10.1038/nn.4611. [PubMed: 28758998]

98. Kang J, Mooshagian E, and Snyder LH (2022). Interhemispheric communication supports bimanual coordination: effects of posterior corpus callosum blockade. Program No. 719.14. 2022 Neuroscience Meeting Planner (Society for Neuroscience). 2022.

99. Mitra PP, and Bokil H (2007). Observed Brain Dynamics (Oxford University Press).

100. Dhamala M, Rangarajan G, and Ding M (2008). Analyzing information flow in brain networks with nonparametric Granger causality. Neuroimage 41, 354–362. 10.1016/j.neuroimage.2008.02.020. [PubMed: 18394927]

101. Mitra PP, and Pesaran B (1999). Analysis of Dynamic Brain Imaging Data. Biophys. J 76, 691–708. 10.1016/S0006-3495(99)77236-X. [PubMed: 9929474]

102. Mikulovic S, Pupe S, Peixoto HM, Do Nascimento GC, Kullander K, Tort ABL, and Leão RN (2016). On the photovoltaic effect in local field potential recordings. Neurophotonics 3, 015002. 10.1117/1.NPh.3.1.015002. [PubMed: 26835485]

103. Peles O, Werner-Reiss U, Bergman H, Israel Z, and Vaadia E (2020). Phase-Specific Microstimulation Differentially Modulates Beta Oscillations and Affects Behavior. Cell Rep. 30, 2555–2566.e3. 10.1016/j.celrep.2020.02.005. [PubMed: 32101735]

104. Tele czuk B, Dehghani N, Le Van Quyen M, Cash SS, Halgren E, Hatsopoulos NG, and Destexhe A (2017). Local field potentials primarily reflect inhibitory neuron activity in human and monkey cortex. Sci. Rep 7, 40211. 10.1038/srep40211. [PubMed: 28074856]

105. Katzner S, Nauhaus I, Benucci A, Bonin V, Ringach DL, and Carandini M (2009). Local Origin of Field Potentials in Visual Cortex. Neuron 61, 35–41. 10.1016/j.neuron.2008.11.016. [PubMed: 19146811]

Highlights

- PRR and LIP encode arm and eye movement plans, consistent with parallel processing streams

- LIP has been implicated in high-level spatial processing, consistent with hierarchical organization

- We found that the causal influence of PRR on LIP is much greater than that of LIP on PRR

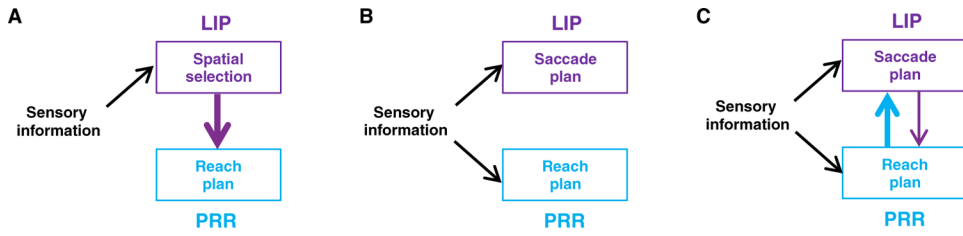- This supports a parallel rather than hierarchical model of information flow in these areas

Figure 1. Models of information flow between PRR and LIP for coordinated eye and arm movements

(A) Spatial hub. If LIP is a hub region that sets spatial priorities for other areas, then we would predict strong information flow from LIP to PRR when preparing a reach (purple arrow). Additional pathways, not shown, would convey information from LIP to other motor and cognitive regions, including saccade planning regions.

(B) Parallel processes. PRR and LIP may each receive sensory information and independently plan reaches and saccades, respectively. In this model, there would be little or no communication between the areas; coordination would occur downstream.

(C) A parallel model with asymmetric interactions. Coordination between reaches and saccades could be accomplished in part via these connections, which would likely be asymmetric (see text). We find strong flow from PRR to LIP and little or no flow from LIP to PRR, in support of this model. A fourth model (not shown) in which information flows from sensory areas to PRR and from PRR to LIP is ruled out by the fact that PRR has reduced activity during a saccade-only task, plus strong evidence that LIP receives substantial input from lower order visual areas.[7,24,41,42]
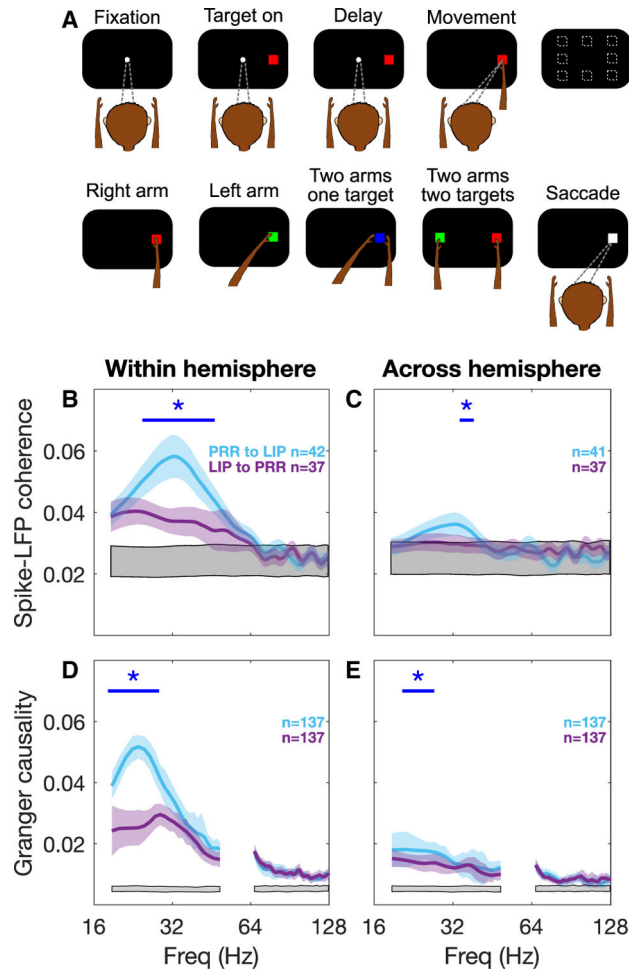
Figure 2. Inferred information flow between PRR and LIP during the planning period for coordinated eye and arm movements

(A) Upper row: animals begin trials by fixating on a central target and placing their hands on home buttons. After 500 ms, a peripheral target appears. The color of the target instructs a particular movement. The target remains on throughout a variable delay period (1,250–1,750 ms). After the delay, the fixation target disappears, instructing the animal to perform the previously instructed movement (go cue). Targets can appear at 1 of 8 possible locations. If an RF is identified, then only 2 target locations are used (1 in the RF and 1 diametrically opposed). Lower row: a red or green target instructs a right or left unimanual arm movement, respectively; the other hand must stay on its home button. A blue target instructs movements of the 2 arms to the same target ("bimanual together"). Simultaneous red and green targets instruct movements to separate targets (i.e., right arm to red and left arm to green; "bimanual apart"). Simultaneous targets always appear diametrically opposite to one another. Except for bimanual apart trials, the animal is required to make an eye movement to the target at the same time as the arm movement. Animals also perform saccade-only trials without arm movements. All 5 trial types are interleaved.

(B) Within-hemisphere spike-LFP coherence is significantly higher from PRR to LIP than vice versa at 25–45 Hz. The blue asterisks and bar denote $p < 0.001$ (pooled t-test). Colored shaded regions denote ±1 SEM. The gray-shaded region represents the 99% bounds of a

shuffle test (see STAR Methods). Peak PRR-to-LIP coherence is 0.060 at 32 Hz, whereas peak LIP-to-PRR coherence is 0.043 at 20 Hz. Measured from the chance level of 0.024, this is a ratio of >2:1. Only reach trials are used in this and the following panels. n indicates the number of spike-LFP pairs.

(C) Spike-LFP coherence across hemispheres is significantly higher from PRR to LIP than vice versa at 35–37 Hz.

(D) Similar effects were found using LFP-LFP spectral Granger causality. Within-hemisphere, peak PRR-to-LIP Granger causality was 0.052 at 24 Hz and peak LIP-to-PRR Granger causality was 0.024 at 30 Hz. The blue asterisks denote $p < 0.001$ (Wilcoxon signed rank test). Measured from the chance level of 0.005, this is a ratio of 2:1. n indicates the number of LFP-LFP pairs.

(E) Spectral Granger causality between PRR and LIP across hemisphere. PRR-to-LIP values are significantly higher than vice versa at 21–26 Hz.
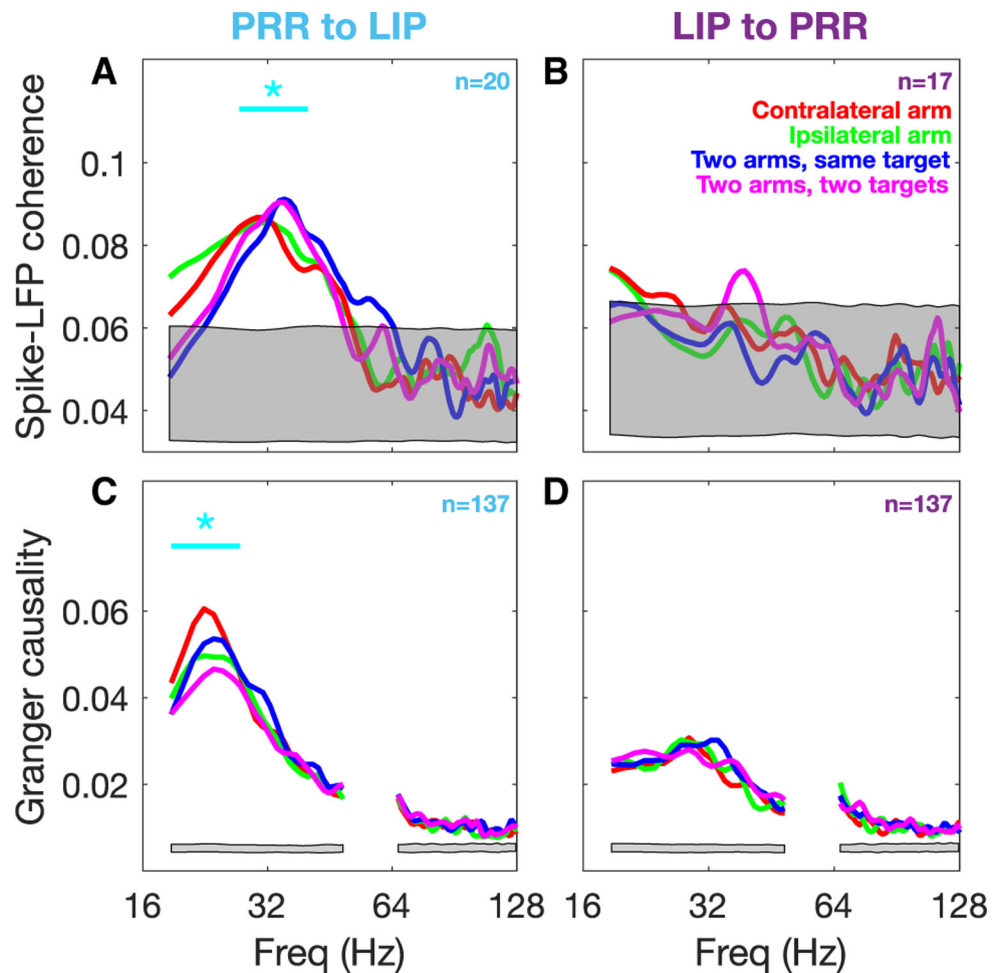
Figure 3. Inferred information flow from PRR to LIP within hemisphere is task-specific

(A) Spike-LFP coherence from PRR to LIP depends on task. Coherence differs significantly across individual tasks at 27–40 Hz (repeated-measures ANOVA, $p < 0.001$). Note that these same frequencies showed significantly greater PRR-to-LIP than LIP-to-PRR coherence when tasks were pooled (Figure 2B). Coherence for the 2 bimanual tasks (blue and purple) peak at 35 Hz (0.091), whereas the 2 unimanual tasks (red and green) peak at 30 Hz (0.087). In each panel, gray-shaded regions represent the 99% bounds of a shuffle test. Cyan asterisks and straight lines indicate frequencies, with a significant variation across reach tasks (repeated-measures ANOVA [$p < 0.001$] for spike-LFP coherence and a permutation test [$p < 0.01$] for spectral Granger causality). n indicates number of spike-LFP or LFP-LFP pairs.

(B) Spike-LFP coherence from LIP to PRR does not depend on the task at any frequency.

(C) Granger causality from PRR to LIP depends on the task, differing significantly across individual tasks from 19 to 27 Hz (permutation test, $p < 0.01$). These same frequencies showed significant asymmetry in Granger causality when tasks were pooled (Figure 2D). Coherence for the 2 bimanual tasks (together and apart) peak at 24 Hz (0.054 and 0.045, respectively), whereas the two unimanual tasks (contralateral and ipsilateral arms) peak at 23 Hz (0.061 and 0.050, respectively).

(D) There was no task-specific modulation in Granger causality from LIP to PRR.
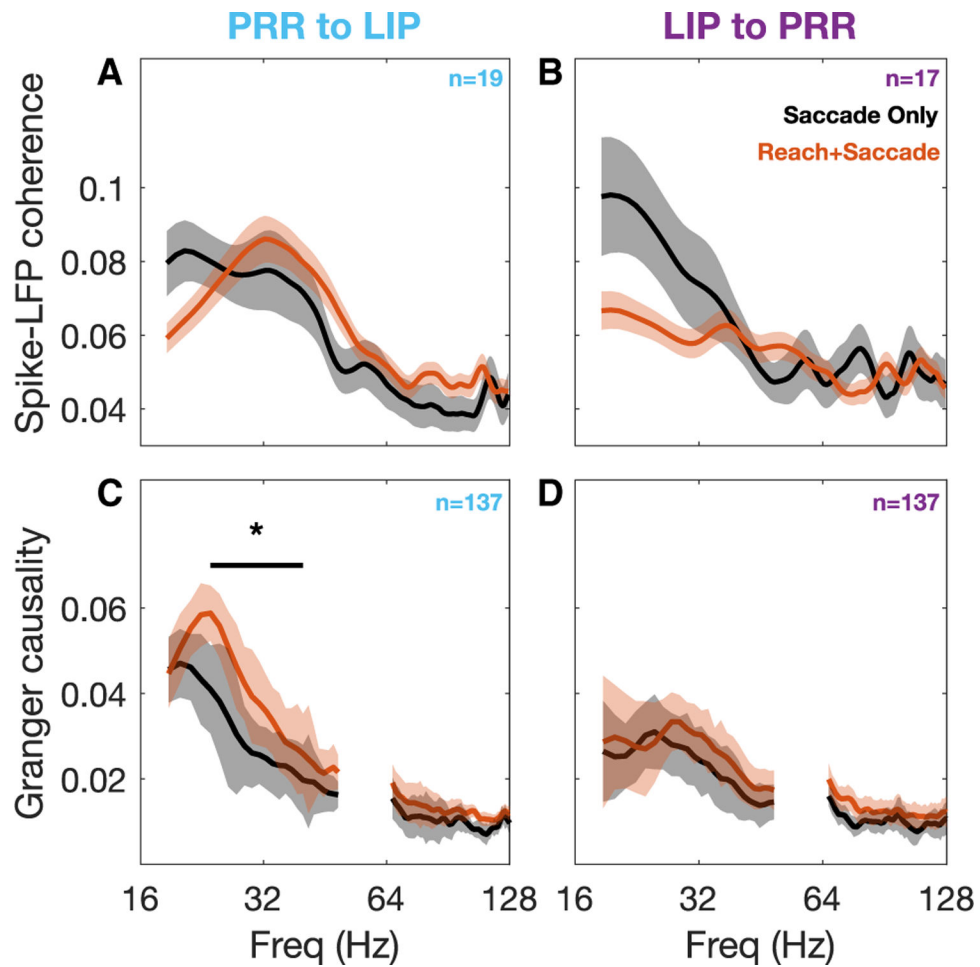
Figure 4. Inferred information flow is effector specific

Inferred information flow during the preparatory period for coordinated reach plus saccade movements (orange) and for saccade-only movements (black). Reach plus saccade movements (orange) include 4 different types of arm movements accompanied by eye movements: unimanual (left or right arm) movements, bimanual movements to a single target (bimanual together), and bimanual movements to 2 targets (bimanual apart). Although a saccade was not required in bimanual apart trials, animals almost always executed a saccade to one or the other target.[72]

(A and B) Spike-LFP coherence for (A) PRR to LIP and for (B) LIP to PRR. Shading indicates ±1 SEM; n indicates the number of spike-LFP pairs.

(C and D) Spectral Granger causality for (C) PRR to LIP and for (D) LIP to PRR. Only Granger causality from PRR to LIP shows a significant difference (asterisks and straight lines, Wilcoxon signed rank test, $p < 0.01$), but power is limited compared to all of the other analyses in this study (see text). Shading indicates ±1 SEM; n indicates the number of LFP-LFP pairs.
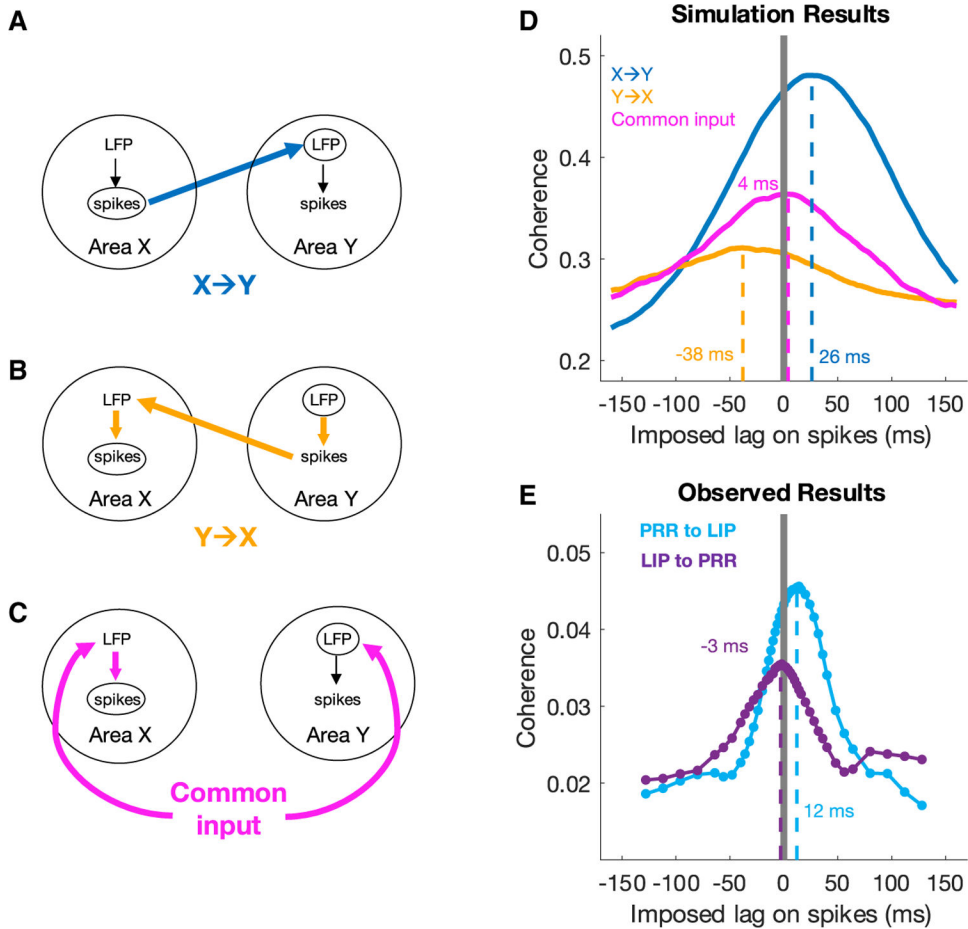
Figure 5. Time-lagged spike-LFP coherence analysis differentiates patterns of information flow

There are 3 ways that spikes originating from one area (X) may be coupled to LFP recorded from a second area (Y). Consider 3 different types of information flow between areas X and Y (A)–(C). In each condition, we recorded spikes in area X and LFP in area Y (small ovals). All within-hemisphere data from all of the tasks are included, although similar effects were observed if only the 4 reach tasks were used, as in Figures 2 and 3.

(A) Information may flow from area X to area Y (blue arrow), directly coupling spikes in X with LFP in Y (small ovals). The coupling is direct because some of the spikes recorded from X may directly drive LFP recorded in Y.

(B) Information may flow from area Y to area X (orange arrows), weakly coupling spikes in X with LFP in Y (small ovals). The coupling is much weaker than in (A) because it involves 3 steps. The recorded LFP (from Y) may drive spikes in Y. Some of these spikes may in turn drive LFP in X. Finally, LFP in X may drive the recorded spikes (in X).

(C) Information may flow from a third common area into both area X and area Y (magenta arrows), coupling spikes in X with LFP in Y (small ovals). Coupling involves 2 steps: LFP in X will resemble the recorded LFP in Y, since both are driven by a common source. LFP in X will drive recorded spikes (in X). Coupling strength is likely to be intermediate between (A) (single step) and (B) (3 steps).

(D) Time-lagged coherence analysis for the information flows shown in (A)-(C), obtained by simulation. See STAR Methods and Figure S10 for simulation details. The time-lagged analysis imposes a lead or lag on spikes before computing coherence. The amount of imposed lag is plotted on the X axis, and the resulting spike-LFP coherence is plotted on the Y axis. With flow from area X to Y (A, blue trace in D), maximal coherence occurs when a lag is imposed on spikes relative to LFP that exactly compensates for conduction times and synaptic delays in the pathway from area X to area Y. Coherence is strong because spikes in X directly influence LFP in Y. With flow from area Y to X (B), the direction is reversed: spikes in X are indirectly influenced by the LFP in area Y. As a result, maximal coherence occurs when a lead (a negative lag) is imposed on spikes relative to LFP (orange trace in D). Since the linkage is indirect (see B), coherence is weaker than in the direct case (orange versus blue). Finally, common input into areas X and Y directly influences LFP and indirectly influences spikes (C). Maximal coherence between spikes in X and LFP in Y occurs when a small lead is imposed on spikes relative to LFP (magenta trace in D). Peak coherence is intermediate between the other 2 cases.

(E) Time-lagged coherence analysis from neuronal recordings. As in (D), coherence is plotted as a function of the imposed lag on spikes. For PRR to LIP (cyan), maximal coherence occurs with an imposed lag of 12 ms, consistent with direct communication (e.g., A). For LIP to PRR (purple), maximal coherence occurs with an imposed lead of 3 ms and has a lower peak value (0.034 versus 0.044). This is consistent with an indirect effect of the strong PRR to LIP flow (as in B) plus (1) common input (as in C), (2) a small amount of LIP-to-PRR flow, or (3) some combination of (1) and (2). See Figure S10 for details. Data for (E) are from within-hemisphere recordings from all of the tasks, although similar effects are seen if only the 4 reach tasks are used. Coherence is computed centered at 25 Hz with broad frequency smoothing.
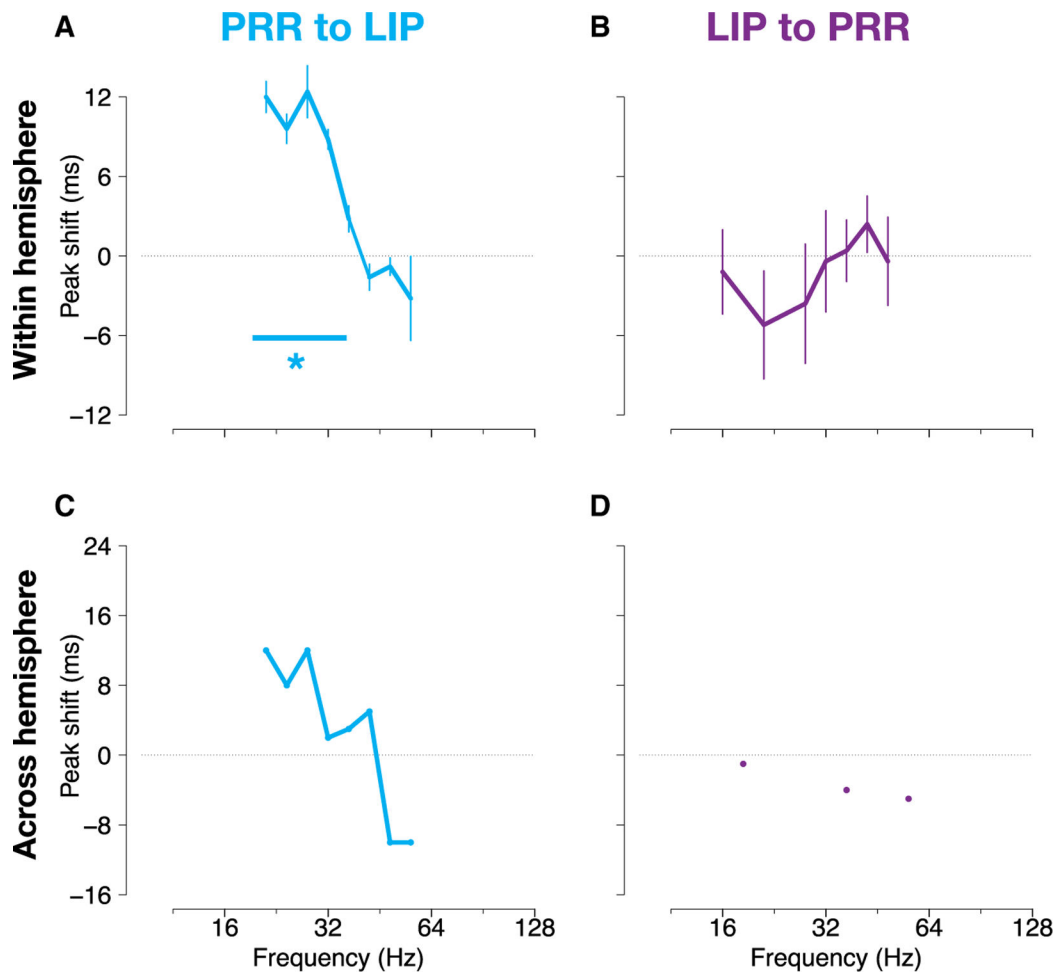
A PRR to LIP
B LIP to PRR

C
D

Figure 6. Timed-lagged spike-LFP coherence analysis across different frequencies between PRR and LIP

For each direction of communication, from PRR to LIP (cyan), and from LIP to PRR (purple), and for connections within (A and B) and across hemispheres (C and D), we used time-lagged coherence analysis to compute peak lag at each frequency (see Figure 5 for details).

(A) Spikes recorded in PRR and LFP recorded in LIP from the same hemisphere. At 21–36 Hz, there is a significant ~10-ms peak lag (2-tailed t test [$p < 0.05$]), consistent with information flow from PRR to LIP. For (A) and (B), we computed peak lags separately for each task type and then plotted data only for those frequencies in which the peak lags for all 5 task types were more similar than would be expected by chance (permutation test, $p < 0.001$). Error bars denote ±1 SEM. A narrow frequency bandwith was used, compared to Figure 5E, to increase frequency resolution.

(B) Spikes recorded in LIP and LFP recorded in LIP from the same hemisphere. At 21–36 Hz, there is no lag but instead a lead of ~4 ms ($p > 0.05$). This is again consistent with information flow from PRR to LIP (see Figure 5).

(C) Similar to (A), but across hemispheres. At 21–36 Hz, there is a clear peak of ~10-ms lag, consistent with information flow from PRR to LIP. Cross-hemisphere coherence was much weaker than within-hemisphere coherence (see Figures 2B and 2C). Therefore, for (C) and

(D), we merged task types together before computing coherence and plotted data only for those frequencies in which there was a well-defined peak in the data.

(D) Similar to (B), but across hemispheres. At most frequencies, there was no consistent peak. A few frequencies between 21 and 36 Hz showed peaks close to 0 ms, consistent with common input.
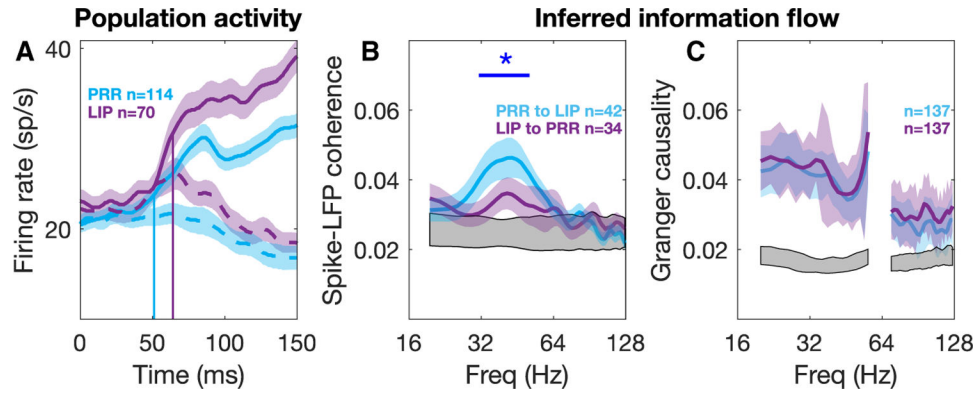
Figure 7. PRR and LIP firing rates and inferred information flow immediately following target appearance

(A) Spike activity in PRR (cyan) reflects directional information about an upcoming reach earlier than in LIP (purple). Mean firing rates are aligned on the appearance of a target cueing a combined reach and saccade. Preferred and null direction responses (solid and dashed traces, respectively) separate after 50 ms for PRR (cyan vertical line) and after 61 ms for LIP (purple vertical line) (paired t test, first of at least 10 consecutive 1-ms frames with t test, $p < 0.01$ in each frame). Data are from 114 PRR and 70 LIP cells and across each of 4 different single trial tasks. Similar results were obtained for each individual animal (53 versus 67 ms for 74 PRR and 45 LIP cells in monkey Z, and 71 versus 88 ms for 40 PRR and 25 LIP cells in monkey T). Shading denotes ±1 SEM.

(B) Spike-LFP coherence between PRR and LIP in the same hemisphere. Peak PRR-to-LIP coherence was 0.046 at 43 Hz, whereas peak LIP-to-PRR coherence was 0.036 at 41 Hz. Measured from the chance level of 0.024, this is a ratio of >2:1. Colored shading denotes ±1 SEM. Asterisk and line denote $p < 0.001$ (pooled t test). The lower graey-shaded region represents the 99% bounds from a permutation test.

(C) Spectral Granger causality between PRR and LIP in the same hemisphere with similar format as in (B).

KEY RESOURCES TABLE

REAGENT or RESOURCE	SOURCE	IDENTIFIER
Deposited Data		
Single unit, LFP, spike-LFP coherence and LFP-LFP Granger causality between PRR and LIP	Current manuscript	https://doi.org/10.5281/zenodo.10811347
Experimental models: Organisms/strains		
Rhesus macaques		Macaca Mulatta
Software and algorithms		
Chrounx	Chronux Developers	http://chronux.org/
Fieldtrip	Fieldtrip Developers	https://www.fieldtriptoolbox.org/
MATLAB	Mathworks	https://www.mathworks.com/
R	The R Foundation for Statistical Computing	https://www.r-project.org/
Original code for data analysis	Current manuscript	https://doi.org/10.5281/zenodo.10811347